Impact ionization mass spectra of anorthite cosmic dust analogue particles

JOURNAL OF GEOPHYSICAL RESEARCH, VOL. ???, XXXX, DOI:10.1029/,

Impact Ionization Mass Spectra of Anorthite Cosmic Dust Analogue Particles

J. K. Hillier,[1,3,7] F. Postberg,[2,3,5] S. Sestak,[1,4] R. Srama,[2,5] S. Kempf,[2,6,7]

M. Trieloff,[3], Z. Sternovsky,[7] and S. F. Green[1]

Abstract. Anorthite, the Ca-rich endmember of plagioclase feldspar, is a dominant mineral component of the Lunar highlands, Plagioclase feldspar

---

S. F. Green, Planetary and Space Sciences Research Institute, The Open University, Milton Keynes, Buckinghamshire, MK7 6AA, UK. (s.f.green@open.ac.uk)

Jon. K. Hillier, Institut für Geowissenschaften, Universität Heidelberg, Im Neuenheimer Feld 234-236, D-69120 Heidelberg, Germany (jonathan.hillier@geow.uni-heidelberg.de)

S. Kempf, LASP, 1234 Innovation Drive, Boulder, Colorado, USA. (sascha.kempf@lasp.colorado.edu)

F. Postberg, Max Planck Institut für Kernphysik, Saupfercheckweg 1, 69117 Heidelberg, Germany. (frank.postberg@mpi-hd.mpg.de)

S. Sestak, Commonwealth Scientific and Industrial Research Organization, Petroleum Resources, PO Box 136, North Ryde, Sydney, NSW 1670, Australia. (stephen.sestak@csiro.au)

R. Srama, Max Planck Institut für Kernphysik, Saupfercheckweg 1, 69117 Heidelberg, Germany. (ralf.srama@mpi-hd.mpg.de)

Z. Sternovsky, LASP, 1234 Innovation Drive, Boulder, Colorado, USA. (zoltan.sternovsky@lasp.colorado.edu)

M. Trieloff, Institut für Geowissenschaften, Universität Heidelberg, Im Neuenheimer Feld 234-236, D-69120 Heidelberg, Germany. (mario.trieloff@geow.uni-heidelberg.de)

[1]Planetary and Space Science Research Institute, The Open University, Walton Hall, Milton Keynes, MK7 6AA, UK.

is also found in comets, meteorites and stony asteroids. It is therefore expected to contribute to the population of interplanetary (and circumplanetary) dust grains within the solar system. After coating micron- and submicron-sized grains of Anorthite with a conductive layer of Platinum, the mineral was suc-

[2]Max Planck Institut für Kernphysik, Saupfercheckweg 1, 69117 Heidelberg, Germany.

[3]Institut für Geowissenschaften, Universität Heidelberg, Im Neuenheimer Feld 234-236, D-69120 Heidelberg, Germany.

[4]Current address: Commonwealth Scientific and Industrial Research Organization, Petroleum Resources, PO Box 136, North Ryde, Sydney, NSW 1670, Australia.

[5]Insitut für Raumfahrtsysteme, University of Stuttgart, 70569 Stuttgart, Germany.

[6]Technische Universität Braunschweig, Braunschweig, Germany.

[7]LASP, University of Colorado at Boulder, USA

cessfully accelerated to hypervelocity speeds in the Max Planck Institut für Kernphysik's Van de Graaff accelerator. We present impact ionization mass spectra generated following the impacts of anorthite grains with a prototype mass spectrometer (the Large Area Mass Analyser, LAMA) designed for use in space, and discuss the behavior of the spectra with increasing impact energy. Correlation analysis is used to identify the compositions and sources of cations present in the spectra, enabling the identification of several molecular cations (e.g. $CaAlO_2$, $CaSiO_2$, Ca_2AlO_3/$CaAlSi_2O_2$) which identify anorthite as the progenitor bulk grain material.

1. Introduction

The in situ compositional analysis of interplanetary, circumplanetary and interstellar dust grains can provide valuable and unique information about the composition and physical state of their source bodies or regions. For example, dust detectors have been used to investigate the composition of cometary dust (*Kissel et al.* [2004, 1986a, b]; *Kissel and Krueger* [1987a], *Langevin et al.* [1987]), interplanetary and interstellar dust [*Hillier et al.*, 2007a; *Altobelli et al.*, 2006; *Grün et al.*, 1980], volcanic dust from Io [*Postberg et al.*, 2006], stream dust from the Saturnian system [*Kempf et al.*, 2005], the composition of Saturn's E ring [*Hillier et al.*, 2007b; *Postberg et al.*, 2008] and the composition of the interior of Enceladus [*Postberg et al.*, 2009a, 2011a].

With the exception of the dust detector onboard the Rosetta spacecraft (COSIMA, *Kissel et al.* [2007]), all other spacecraft-based dust analyzers thus far have relied upon impact ionization time of flight mass spectrometry (TOF-MS) when determining the composition of encountered dust grains. In their most basic forms, these spectrometers rely on the relationship between the flight time of an ion, from its point of creation until its subsequent detection, to the charge to mass ratio of the ion. Generation of a mass scale from the flight time domain (using e.g. $t_i = a\sqrt{m_i/q_i} + b$, where a is known as the stretch parameter and b as the shift parameter, t_i, m_i and q_i represent the arrival time, mass and charge of a particular ion species, i) is then possible, assuming that the ions of different masses possess the same initial energy distribution. Early instruments, such as the micrometeoroid experiment on the Helios spacecraft [*Dietzel et al.*, 1973], used a simple drift tube arrangement and plasma separating electric field to obtain low resolution ($\frac{m}{\Delta m} \approx 5 - 10$)

mass spectra [*Altobelli et al.*, 2006]. Improved electronics and field geometries, such as those used for Cassini's Cosmic Dust Analyzer (CDA, *Srama et al.* [2004]) improved the mass resolution (to $\frac{m}{\Delta m} \approx 20 - 50$ for CDA). The mass resolution of these instruments was limited by the length of the drift region and the effects of the ions' initial energy distributions. To help solve these problems a more complicated series of fields is used, known as a reflectron [*Alikhanov*, 1957; *Mamyrin et al.*, 1973].

A reflectron allows longer ion flight times, increasing the mass resolution of the instrument, as well as the removal of the effects of the ions' initial energies. Reflectron technology was used in the Particle Impact Analyzer (PIA) on the Giotto spacecraft [*Kissel et al.*, 1986a], PUMA1 and PUMA2 on the VeGa spacecraft [*Kissel et al.*, 1986b; *Kissel and Krueger*, 1987a] and recently the Cometary and Interstellar Dust Analyzer (CIDA, *Kissel et al.* [2003]) on the Stardust spacecraft, which produced mass spectra with resolutions of up to 250 in laboratory measurements.

To obtain the mass spectra presented here, a next-generation dust impact ionization mass spectrometer was used. Developed by the group at the Max Planck Institut für Kernphysik, the Large Area Mass Analyzer (LAMA, $\frac{m}{\Delta m} \approx 150 - 300$ *Srama et al.* [2007]) is a reflectron-based instrument with a large target area, originally designed for use in low dust flux environments, such as for the detection of interstellar dust. LAMA is capable of operating in both a positive ion mode and a negative ion mode, with dust impacting a silver target and either cationic or anionic species then delivered to an ion detector. A similar instrument has also been developed at LASP, University of Colorado at Boulder, for use in detecting interstellar dust and in a lunar environment [*Sternovsky et al.*, 2007a, b; *Sternovsky et al.*, 2011].

The method utilized by these instruments to produce the initial plasma cloud, namely ionization initiated by the rapid deceleration experienced by the particles during impact, leads directly to difficulties in interpreting the mass spectra produced. The energetics and composition of the cloud of charged and neutral species produced by an impact depend strongly on the impact conditions. These impact conditions include not only the composition and density of the impact target and the impacting dust grain themselves, but also the mass of the impacting grain and the speed at which it strikes the target. Although advances have been made in modeling this process (e.g *Hornung et al.* [1996]; *Hornung and Kissel* [1994]), many aspects remain poorly understood.

1.1. Laboratory Calibration

To aid the interpretation of mass spectra when inferring the initial particle composition, it is therefore vital to obtain calibration data in the laboratory. To this end individual dust particles are usually accelerated in a Van de Graaff accelerator [*Mocker et al.*, 2011; *Shibata et al.*, 2001; *Burchell et al.*, 1999a]. These instruments accelerate charged dust particles to hypervelocities by passing them through a large potential difference ($\approx$ 2 MV). The charged dust grains are then given a velocity (v) related to their charge (q) to mass (m) ratio and the potential difference (V) through which they have passed (this relationship is given by $\frac{1}{2}mv^2 = qV$). Depending on the dust particle size, its charging efficiency and the potential through which it passes, velocities ranging from <1 to >100 km s^{-1} are possible. It should be noted that the dust charging process within the accelerator tends to give individual similar dust grains very similar charges (subject to the field strength remaining below the field emission limit). This similar charging effect means that for a particular dust grain material and size, and a given acceleration voltage, only a limited

velocity range is available.

Acceleration of particles in a Van de Graaff accelerator can only occur if the particles are capable of holding enough charge. Ideally this means that they are conducting, although a conductive surface coating also allows the particles to charge and electrostatically accelerate (e.g. *Burchell et al.* [1999b, 2002]; *Goldsworthy et al.* [2002, 2003]; *Fujii et al.* [2006]; *Srama et al.* [2009]; *Hillier et al.* [2009]). The method used to coat the mineral grains in this work is that described in *Hillier et al.* [2009], itself an adaptation of methods described by *Lee et al.* [2007] and *Chen et al.* [2005]. This involves first functionalizing the mineral grains (generated by hand grinding larger samples using an agate pestle and mortar) by adding a self-assembled monolayer (SAM) of mercaptopropyl trimethoxysilane (MPTMS). The silane group end of the MPTMS molecule has an affinity for hydroxylated oxide surfaces, whilst the mercapto group attracts certain metals. The functionalized particles are then placed in a solution of a platinum salt (potassium hexachloroplatinate in this case) and the adsorbed metal salt molecules subsequently reduced to metallic platinum, creating an exceedingly thin metal layer on the particles. If homogeneous coating is assumed then the layer formed during the initial soak in the Pt salt solution is (at most) a single monolayer. This layer can be thickened by the addition (and subsequent in situ reduction) of further Pt salt.

1.2. Anorthite

The material chosen for the impact ionization experiments described in this work was Anorthite. Anorthite ($CaAl_2Si_2O_8$) is the Na-poor end member of the plagioclase feldspar series, represented at the Na-rich end by Albite ($NaAlSi_3O_8$). Anorthite was chosen for several reasons: as a silicate, it can be readily coated with Pt using the method outlined

above, whereas some other common minerals (e.g. sulfides) require coating with a thin layer of silica prior to metallating; it consists of elements which are both easily ionized (e.g. Ca, Al - see Table 1), and less so (e.g. Si, O), this range of ionization energies, together with differing tendencies to form anions or cations, should result in changes to the mass spectra with different impact conditions; the elements present are not those commonly found as terrestrial contaminants (Na and K are more common contaminant species than Ca in laboratory mass spectra, *Postberg et al.* [2009b]) or used during the coating process (Table 1) and finally, anorthite is of astrophysical relevance.

One of the earliest minerals to condense from a solar composition gas [*Ciesla*, 2010; *Grossman*, 2010] anorthite, or anorthite-rich minerals, have been observed around post-AGB stars [*Matsuura et al.*, 2004]. Within the solar system, anorthite has been observed on the surface of Mercury (e.g. *Sprague et al.* [1997]; *Warell* [2002]; *Sasaki and Kurahashi* [2004]; *Warell et al.* [2010]), and is the most abundant mineral species in the lunar highlands (e.g. *Dowty et al.* [1974]; *Yan et al.* [2010]; *Hargraves and Hollister* [1972]; *Lucey* [2004]; *Ohtake et al.* [2009]; *Wood et al.* [1970]). Anorthite has been found in several classes of meteorites, often linked to Calcium-Aluminium-rich inclusions, but also those believed to have a lunar origin (e.g. *Aléon et al.* [2002]; *Krot and Keil* [2002]; *Demidova et al.* [2003]; *Grossman and Steele* [1976]; *Wark* [1987]). The presence of anorthite in meteorites has been confirmed by the detection of anorthite in asteroid reflectance spectra [*Taylor et al.*, 2007; *Sunshine et al.*, 2008; *Stern et al.*, 2011]. Present on the surface of many atmosphereless bodies, and during the formation of the solar system, anorthite would therefore be expected to be found in interplanetary dust, and this is indeed the case, with interplanetary dust [*Christoffersen and Buseck*, 1986; *Greshake et al.*, 1996]

and cometary dust [*Zolensky et al.*, 2006; *Ishii et al.*, 2008; *Simon et al.*, 2008] featuring the mineral.

2. Experimental Data

The data were collected on the 6th and 9th of March, and the 29th and 30th of April, 2009. A charge detection system (the particle selection unit, PSU) on the Max Planck Institut für Kernphysik's Van de Graaff accelerator measured the charge on each individual mineral grain which traveled down the instrument beam line. From this charge, and the time of flight of the particle within the detector, the mass and velocity of each grain was derived. The mass and velocity distribution of the anorthite grains is shown in Fig. 1. The corresponding impact velocity histogram is shown in Fig. 2. In total 299 positive mode mass spectra with corresponding (PSU-derived) mass and velocity information were obtained, as well as an additional twelve negative mode mass spectra.

The anorthite used here was synthesised by S. Wilson, research chemistry coordinator, in the framework of the USGS Reference Materials project. Commercially available chemicals in the correct stoichiometric ratios were used in the synthesis. After melting the mixture was annealed for 12 hours and crystallised to form a homogeneous agglomerate. The sample used for the dust originates from the outer rim of this agglomerate. More detailed analyses are presented in *Höfer* [2010]. The mass spectra were initially calibrated and processed using in-house software "SpectrumGUI". With this the mass spectra were individually calibrated to determine their shift and stretch parameters. Unlike non-reflectron instruments, such as Cassini's CDA [*Srama et al.*, 2004], spectra produced using LAMA have narrow peaks relatively unaffected by plasma ion energetics. Also, the instrument trigger (recording) time can be determined more reliably than with CDA. The spectra are

therefore considerably easier to calibrate onto a mass scale. Spectra were then aligned, and co-added in velocity bins. The spectra were divided into velocity bins such that there were at least three spectra per bin, with five or more preferred. The mean mass, velocity and charge corresponding to each velocity bin is shown in Table 3, together with the number of spectra per bin and the sum spectrum resolution. Prior to the analysis of this data it was believed that cation spectra were more suitable for the analysis of mineral particles. The collection of cation spectra was therefore prioritised, resulting in too few anion spectra for co-adding and analysis in the same way as the cation spectra. The anion spectra collected were also found to be noisy, with few identifiable features. Thus only the cation spectra will be considered in this work.

The sum spectra were then baseline subtracted using a suitable polynomial fit to the lowest points in each spectrum. For each spectrum the noise level was calculated from a region with no mass lines (3.5–5.5 u and 7.5–9.5 u) and each spectrum was then divided by this to produce spectra in units of signal-to-noise. This process was also performed to create a sum spectrum of all the individual cation spectra.

Co-adding increased the signal-to-noise ratios of the spectra, improving the statistical significance of small peaks. Use of sum spectra was also intended to average out the large scatter observed in peak amplitudes even for extremely similar impact conditions (particle mass and velocity), highlighting general trends.

The "errors" in peak amplitudes for the sum spectra are therefore due to two main sources: instrument noise from the electronics and plasma environment, and variations in ion numbers due to the stochastic nature of the impact process in terms of, for example, energy partitioning and impact parameters (e.g. surface roughness, contaminant levels, particle

orientation). Presenting the sum spectra in units of signal-to-noise is designed to enable a better comparison between sum spectra by removing the effects of changes in instrument noise.

Examples of the degrees of scatter in peak amplitudes for eight common elements (the main isotopes of H, C, Na, Al, K, Ca and both Ag isotopes) due to contamination, particle and/or target material, in the eight spectra created by particles impacting at velocities of between 10 and 10.999 km s^{-1}, are shown in Fig. 3. These amplitudes are shown in their original units (volts), as conversion to the same units used in the sum spectra (signal-to-noise) introduces uncertainty into how much of the scatter may be due to changes in peak amplitude or noise level. This scatter has not been shown as either a range or standard deviation in subsequent figures. Use of a range to show the distribution gives no indication of any trends within the data comprising each sum spectrum. Use of a standard distribution is complicated by the aforementioned choice of units.

However, despite the sometimes small numbers (3 – 49, Table 3) of spectra in each considered speed interval, the trends of line amplitudes and the correlations of different lines with speed can be reliably determined and hence the results of the paper are considered to be reliable. We note that the observed scatter in peak amplitudes between spectra due to apparently similar impact events is as expected and previously observed for this type of experiment.

3. Results

The sum spectrum of the complete cation data is shown in Fig. 4. For clarity the spectrum has been split into five 50 u panels, with the 3σ and 5σ values shown by solid

and dashed horizontal lines respectively. Note the changing scale of the ordinate axes. Selected sum spectra corresponding to the different velocity bins are shown in Figs. 5 - 9. The abscissa scale assumes that the ions contributing to the spectra are singly charged only.

In the following discussion, when used to try to identify their source species, the spectral peak amplitudes were, unless otherwise noted, all those which were at least 3σ above their *local* background. When a peak was not at least this amplitude its abundance was set to zero (e.g. for correlation analysis, velocity thresholds).

4. Analysis

The total sum spectrum (Fig. 4) shows, for masses of $<\approx$90 u, peaks at nearly every possible (integer) mass. This is strongly indicative of the presence of complex organic species within the impact plasma and to be expected given the particle coating method (MPTMS has an aliphatic backbone of $(CH_2)_3$ as well as three methyl groups) and probable target or particle contamination with long-chain hydrocarbons from vacuum pump oil and vacuum grease. These contaminants are primarily likely to be hydrocarbon-based (from vacuum pumps used in evacuating the target chamber and during the freeze drying process) rather than siloxane, although a minor amount of contamination from silicone-based vacuum grease used for ensuring the integrity of vacuum seals may be present. Even simple saturated aliphatic hydrocarbons will produce singly charged cations at masses of C_nH_{2n+1} whereas unsaturated aliphatic hydrocarbons will produce cations with masses of C_nH_{2n-1} and, with rearrangement, C_nH_{2n}. Thus for n = 1–5 one would expect peaks at masses of 15, 29, 43, 57 and 71 u from saturated simple hydrocarbons and 13, 14, 27, 28, 41, 42, 55, 56, 69 and 70 u for unsaturated simple hydrocarbons. The addition

of O, Si and S in the coating process allows for further permutations of cation peaks, unrelated to the particle material, to appear in spectra (see for example *Mellado et al.* [2011]). Reference electron ionisation mass spectra of MPTMS show significant (greater than 5% of the most intense peak) peaks at masses of (in u, with the most abundant peak in bold): 59, 61, 90, 91, 92, 93, 106, **121**, 122, 123, 125, 133, 136, 164, 165, 166. Na and K peaks due primarily to anthropogenic contamination also often occur in impact spectra (e.g. *Postberg et al.* [2009b]). This complicates the unambiguous identification of species, both atomic and molecular, due to the particles' original mineral composition. Mineral assay data (Table 2) showed that, prior to coating, the anorthite grains were very low in Na, Mg, K and Fe. The grains were dominated by Al, Si, Ca and O.

There are five main ways to identify peaks in mass-calibrated impact ionisation mass spectra:

1. Direct identification based on unambiguous mass assignment. This is particularly possible with low mass species (e.g. H, H_2, H_3, Li, B, C) as they cannot be confused with any other singly-charged ions. Species with unique isotope patterns (e.g. Li, B, Ag, Pt) are also easy to identify providing there are no other contributions to any of their mass lines. Ions with higher masses which do not have plausible isobars can also be assigned to the most likely species. Finally it is possible to unambiguously identify ions which are formed from clusters of the bulk target element with those of the bulk projectile. These clusters, observed in Cassini CDA data [*Kempf et al.*, 2005; *Postberg et al.*, 2006; *Hillier et al.*, 2007a, b], are particularly useful in the case of LAMA spectra as the isotope pattern of the Ag target is echoed by the cluster ions.

2. Appearance with impact velocity. The impact velocity threshold at which a peak appears in a spectrum can be used to help infer the identity of the ion. Species which are detectable at very low velocities must have low ionisation energies together with a tendency to form cations (if positive mode spectra are being recorded). The alkali contaminant ions of Na and K are the most common example of this. Species detected at low impact velocities are also more likely to be molecular, as too little energy is available to completely fragment the parent molecules. Species with higher ionisation energies, or which prefer to form anions (such as Cl, N) will, if they are abundant enough in the impact plasma, tend to appear at higher impact velocities (e.g. > 20 km s^{-1}).

3. Disappearance with impact velocity. At higher velocities more energy is concentrated into a smaller impact region. This increase in energy density produces plasma conditions which break up molecules and thus decreases the abundance of molecules in the spectra. However, the energy regime in which Van de Graaff accelerated particles exist biases the initial abundance of species within the impact plasma. From the fit line in Fig. 1 the particle mass scales with $v^{-2.941}$. For a constant particle density the particle volume scales similarly, while the particle surface area will scale with $\approx v^{-1.96}$. The available abundances of species present on the surface of the particles (or the target surface) therefore decreases more slowly than the abundance of a species present as a component of the particle bulk material, with increasing impact velocity. This effect will be complicated by the degree of ionization that the particle surface (or target surface) undergoes versus that of the particle volume.

4. Correlation between peak amplitudes with velocity. Investigating the trends between the amplitudes of different peaks with impact velocity may show links between particular

species. This is of greater use when one species which correlates is identified, although it can also indicate groups of spectral lines which may be linked. Care must be taken due to the large number of factors which may affect peak amplitudes and the appearance of spectral lines.

5. Comparison with results from other mass spectrometry methods. Other methods of producing mass spectra from similar materials can provide valuable clues for identifying (or confirming the identity of) those produced during the impact ionisation process. In particular Secondary Ion Mass Spectrometry (SIMS), Spark Ionization mass spectrometry, Electron Impact mass spectrometry, Matrix-Assisted Laser Desorption/Ionisation Time of Flight mass spectrometry (MALDI-TOF) and Laser Ionization TOF mass spectrometry may all produce spectra with features which are similar to those generated by hypervelocity impact ionization. For example, a comparison of Cassini CDA mass spectra with those produced by Laser-TOF analysis of salt-water mixtures helped determine the original composition of E ring particles originating from within Enceladus [*Postberg et al.*, 2008, 2009a].

There are several origins for species observed within these impact spectra: the particle bulk composition (molecules and atoms containing/of Ca, Al, O, Si), the particle coating and processing (H, C, O, Si, S, Na, K, B, Cl, Pt), the impact target bulk material (Ag) and contamination on the impact target surface (H, C, O, Li, Na, K, Cl). In many cases spectral peaks may show contributions from two or more of these sources, and from different species with the same, or similar, masses. The relative strength of these contributions may also vary with impact velocity.

We directly identify ^{1}H, $^{2}H_2$, $^{3}H_3$, ^{6,7}Li, ^{10,11}B, ^{12}C, ^{13}CH, ^{23}Na, ^{39}K, ^{107,109}Ag,

^{194,195,196,198}Pt and $^{214,216,218}Ag_2$ within the spectra. At 107 and 109 u, the Ag peaks are extremely unlikely to be affected by organic contaminants and can be used to investigate the impact-by-impact sensitivity of the spectrometer. Fig. 10 indicates that at lower velocities there is a larger scatter in the recorded amplitude ratios of the silver ion peaks, but the 109 u peak is generally underrepresented with respect to the 107 u peak. There is no apparent trend with velocity or with the overall amplitudes of the peaks, indicating that the effect is purely due to chance rather than long-chain organic contaminant ions. Despite the lack of a trend with peak amplitudes, it is possible that saturation of the ion detector (micro-channel plate, MCP) contributes to this effect. Assuming the variation in the expected percentage abundances of the Ag ions is repeated at other masses, we infer that recorded peak amplitudes may fluctuate randomly, or due to MCP saturation, by up to ≈4% in amplitude.

AgX^+ target-projectile cluster ions are observed at masses of 147/149 u, 151/153 u and 163/165 u (just below 3σ but clearly identifiable). These correspond to X = 40, 44 and 56 u respectively. These are possibly due to $^{40}Ca^+$, $AlOH^+/SiO^+/^{44}Ca^+$ and $CaO^+/^{28}Si_2{}^+/AlSiH^+$. Clusters of target material atoms with molecular species from the projectile have been previously observed in CDA data obtained in Saturn's E ring [*Hillier et al.*, 2007b], where Rh target atoms clustered with the extremely abundant hydronium-water clusters from the impacting water ice particles. There are no indications of target-projectile clusters of Ag with pure O, Si or Al however. From the lack of common organic ions at 40 u (C_3H_4 is unlikely to be present in large quantities), the early appearance in spectra at low velocities and continued appearance at higher impact velocities (Fig. 13), and the target-projectile cluster ions we therefore identify the source

of the peak at 40 u as primarily ^{40}Ca.

The peak at 16 u appears at the extremely low impact velocity of 0.5 km s^{-1} but then is not detected until 9.5 km s^{-1} (Fig. 12). This behavior is more consistent with the parent species for higher velocity impacts being O rather than CH_4 or NH_2, due to the high ionisation energy of O. The low velocity appearance may be due to pre-impact charge transfer [*Sysoev et al.*, 1997; *McDonnell et al.*, 2001; *Austin et al.*, 2003] generation of O ions, or the organic molecular candidates. The continued increase in the abundance of the 16 u peak with increasing impact velocity also indicates that the species is monatomic and abundant, as would be expected for a component of both the organic coating, contamination and the mineral. The threshold velocities at which different mass species appear in spectra and then become undetectable are shown in Table 5.

Definitively identifying Si as the source ion for the 28 u peak is also complicated by the concomitant appearance of $C_2H_4^+$ at this mass. Spectral features due to the heavier isotopes of Si, at 29 and 30 u (4.68% and 3.09% abundance respectively) may be confused with those from $C_2H_{5-6}^+$ and other molecular organic species. However, the abundances of the heavier Si ions mean that, with a high enough Si signal, they should be detectable in spectra at all impact velocities, whereas the molecular organics should decrease in abundance. By comparing the relative abundances of the 28, 29 and 30 u features, normalised by the sum of their abundances (Fig. 14) it can be seen that the 29 u feature is overabundant at low velocities but then, where detectable, decreases towards the expected abundance for ^{29}Si at velocities greater than 13 km s^{-1}. The relative abundance of the 30 u feature behaves similarly, whereas that of the 28 u feature increases with impact velocity. Therefore the dominant source of the 28 u feature at higher velocities is ^{28}Si,

with contributions from organic species at velocities < 13 km s^{-1}. The reduction in the contribution of organic ions to the 29 and 30 u features with increasing impact velocity then allows the peak amplitudes to approach those which would be expected for purely Si.

The dominant metal ion in anorthite, Al, will occur in the spectra at the same mass (subject to the resolutions of the spectrometer and co-added spectra) as $C_2H_3^+$. The abundance of both species will be expected to decrease with impact velocity, due to the reduction in particle size and the break up of the organics. However, the behaviour of any 27 u organic species with velocity can be estimated by comparing with that of a known organic feature (for low velocities, C_2H_5 at 29 u) and the ^{40}Ca, identified as from the anorthite. Figs. 16 and 11 show that the 27 u feature behaves in a remarkably similar way to that of the Ca with velocity, appearing at the same velocity with high abundance. The 29 u feature appears at low velocities and is far less abundant than either the Ca or the 27 u peak. If the 27 and 29 u features were both dominantly organic their abundances would be expected to be similar and vary similarly (e.g. *Srama et al.* [2009]). We therefore identify the 27 u feature as predominantly due to ^{27}Al, even at low impact velocities.

Having identified the main atomic components of anorthite (Al, Ca, Si and O) within the spectra, we now investigate the 44 and 56 u species indicated by target-projectile clusters. Based on the structure of anorthite [*Taylor and Brown*, 1979], the 44 u species may be due to SiO^+ or $AlOH^+$. The 56 u species may be Si_2^+, $AlSiH^+$ or CaO^+. The 44 u isotope of Ca (2.09%) may also contribute to the 44 u peak. As most of these species are polyatomic, their abundances will decrease with increasing impact velocity in the same way as the abundances of organic contaminant ions (e.g. C_3H_8, SC, C_4H_8). However, previous

TOF-MS of mineral ions generated by laser desorption [*Erel et al.*, 2003; *Sullivan et al.*, 2007] indicate that in Ca, Al and/or Si-rich minerals SiO, CaO cations are formed. Si_2 may also form, depending on the plasma conditions. Although in some publications AlO is shown to form anions [*Sullivan et al.*, 2007; *Trimborn et al.*, 1998; *Jeong et al.*, 1995], AlOH might form a cation at 44 u in impact ionisation spectra. The high abundances of the 44 and 56 u species implied by the existence of target-projectile cluster ions [*Hillier et al.*, 2007b; *Postberg et al.*, 2008; *Kempf et al.*, 2005] indicate that we are indeed detecting significant contributions from ^{44}Ca/SiO/AlOH at 44 u and Si_2/CaO (and possibly AlSiH) at 56 u.

Easily ionised, abundant, at a mass not prone to significant organic contamination, and indicated by elemental peaks, fragment peaks and target-projectile cluster peaks, Calcium is confidently identified as a mineral component in the spectra. To rapidly identify other species which correlate with Ca, and thus may be mineral features in the spectra, we search for statistical trends linking the behaviour of the abundance of Ca in the spectra at different impact velocities with the abundances of other peaks. Two methods were employed to search for trends, namely the calculation of both Pearson and Kendall correlation coefficients. It is important to note that use of correlation techniques in this way involves making the a priori assumption that the composition of the particles is constant, regardless of size. As the anorthite used here is artificial and generated by a melt technique, this assumption is reasonable and supported by SEM investigations of large fragments and small grains of the material [*Höfer*, 2010]. The Pearson correlation coefficient provides a measure of the linear (both direct and inverse) correlation between two data sets. The Kendall (tau) correlation coefficient indicates correlations between ranked

data and, as such, will indicate non-linear correlations as well as linear. It will therefore, with a complex data set, indicate larger numbers of correlations than the Pearson method, but it may be sensitive to the effects of particle size on the abundances of the peaks. In this work, the correlation indicated by the Pearson method was assumed to be reliable if the correlation coefficient >0.423, indicative of a two-tailed confidence of 95%. The correlation indicated by the Kendall method was assumed reliable if it had $p < 0.05$ (i.e. 95% confidence). Correlation analysis was only performed for those species which appeared in at least 25% of the sum spectra.

Pearson correlation coefficients indicate correlations of ^{40}Ca with: Li, Na, Al, 28 u, 29 u, 30 u, K, ^{44}Ca/SiO/AlOH, 50 u, Si_2/CaO, 57 u, 64 u, 65 u, 66 u, 83 u, 96 u, 99 u, 100 u, 112, 113, 117, 147, 155 and the Ag_2 ions. The Kendall correlation coefficients indicate correlations of ^{40}Ca with those indicated by the Pearson coefficient, as well as: H_3, 41 u and 55 u. The correlation of Ca with the easily ionised Li, Na and K is perhaps not surprising, despite the lack of these elements in the mineral, given the ubiquity of these elements. The correlation with all of the 28, 29 and 30 u features is a little strange, given the behaviour of the 29 u feature when compared with the 28 feature (Fig. 14) but may be a consequence of the influence of the Si isotopes on the 29 and 30 u peak amplitudes at higher impact velocities. The 41 u feature may be due to ^{41}K or perhaps an organic contaminant ion such as C_3H_5. Fig. 15 shows the fractional isotopic abundance of the 41 u feature assuming that it is ^{41}K, together with that expected for ^{41}K. Although noisy, there is good agreement, implying that the 41 u feature is primarily due to ^{41}K. The 50 u feature is extremely weak and does not correspond to any common organic fragment mass, nor is it present in the mass spectrum of MPTMS (Spectral Database for Organic Compounds,

http://riodb01.ibase.aist.go.jp/sdbs/cgi-bin/cre_index.cgi?lang=eng). It may possibly be $NaAl^+$, but that identification is very tentative.

The region from 55–57 u shows three features which correlate with Ca, with the 56 u peak already identified. The 55 u feature appears at low impact velocities and then rapidly diminishes (Fig. 17), implying it is easily ionised, initially more abundant and then broken up (or unable to form) at higher velocities. It may be $AlSi^+$ or possibly C_4H_7. The 57 u species is extremely abundant and likely to be protonated molecules of the 56 u species - in particular CaOH [*Silva et al.*, 2000; *Erel et al.*, 2003; *Bruynseels and Van Grieken*, 1983], perhaps with minor contributions from C_4H_9. The 64, 65 and 66 u species (Fig. 18) appear at low velocities and become undetectable at impact velocities of >16 km s^{-1}. No obvious projectile species occur at these masses, so they may be due to stable organic species such as cyclic $C_5H_{4,5,6}$ (e.g. *Srama et al.* [2009]), or to coating organics. The amplitudes of these species are very low, near the statistical noise limit, however Fig. 18 clearly shows that the species appear together in spectra. The 83 u feature is probably due to the addition of Al to the 56 u species, resulting in AlCaO, Si_2Al or Al_2SiH. The 96, 112 and 113 u species are all seen in laser desorption experiments of Ca-rich minerals [*Sullivan et al.*, 2007; *Gallavardin et al.*, 2008; *Bruynseels and Van Grieken*, 1983; *Struyf et al.*, 1998] and are assigned to Ca_2O, $(CaO)_2$ and $(CaO)_2H$ respectively. Clusters of ^{40}Ca with the Si_2 and AlSiH ions at 56 u may also contribute to the 96 u feature. *Jeong et al.* [1995] observe $KAlO_2$ cations in mass spectra of zeolites and we suggest that similar $CaAlO_2$ and $CaSiO_2$ ions are responsible for the 99 and 100 u peaks. The 117 u peak may be due to $CaSiO_3H$. The 147 peak we have already identified as $^{107}AgCa$, although the corresponding correlation with $^{109}AgCa$ is below our selection threshold, possibly due to

the lower abundance of the ^{109}Ag peak and thus a corresponding lower abundance of the associated Ca cluster ion. Although a large peak at 156 u is observed in a mass spectrum of a Li, Na, Al and Ca rich silicate particle [*Silva et al.*, 2000], no definitive identification is given other than to say the isotope pattern of other peaks in that area are consistent with a molecule containing silicon. We explain the large 155 u feature as Ca_2AlO_3 or $CaAlSi_2O_2$, comparable to the 156 u feature in *Silva et al.* [2000] being interpreted as Ca_2SiO_3 or $Ca_2Si_3O_2$. Similarly, the 163 u peak, earlier identified as a target-projectile cluster of Ag with a 56 u species, may have minor contributions from $AlSi_2O_5$ based on structural similarities with species observed in *Silva et al.* [2000] and *Tsugoshi et al.* [1991]. Other features in the spectra may be due to ions derived from the anorthite grains, however, without a compelling argument based on either isotope patterns, lack of (resolution dependent) isobaric compounds at specific masses, comparison with published results using laser ionisation or the presence of target-projectile ions, we do not attempt to conclusively identify them. Also, the contaminated nature of the experimental environment will have introduced hydrocarbon ions which will contribute to a greater or lesser extent to these features. We note that they may also contribute to those features we have identified above, but to a lesser extent, with all major features identified here with confidence (Table 4).

5. Discussion

An important part of determining the composition of dust particles detected in space is the ability to distinguish between components (whether mineral or not) of the particles. The coated anorthite particles here are good analogues for cosmic dust particles consisting of a core-shell morphology, with a mineral core and an organic and metal-rich shell. Once

a particular ion species is identified then, in the absence of a known impact velocity, the laboratory-derived velocity thresholds at which species appear in, and disappear from, spectra can be used to estimate particle velocity. This relies upon assumptions that the particle mass-velocity ratio is similar to that produced in the Van de Graaff, or that the appearance thresholds are largely independent of composition and the charge on the particle and predominantly dependent on impact velocity.

Similarly, if the impact velocity is known then the appearance and disappearance thresholds of a species in spectra may be used to infer the probable identification of the species, should (resolution dependent) isobaric species exist.

Some of the generation mechanisms of plasma produced by hypervelocity impacts are believed to differ from those produced by laser ionization [*Kissel and Krueger*, 1987b; *Kissel and Krueger*, 2001]. However, the ions produced, including the molecular fragment and cluster ions, are found to be similar, with production processes presumably dominated by their bond strengths, ionization energies, electron affinities and oxidation states.

Some results from laser ionization experiments with minerals indicate that Al-oxide and Si-oxide species, and their clusters, will tend to form negatively charged ions [*Jeong et al.*, 1995; *Trimborn et al.*, 1998; *Sullivan et al.*, 2007; *Xu et al.*, 1998, 1997]. The absence of high abundances of ions with masses corresponding to these species in the cation mass spectra presented here tends to confirm that this effect also occurs in impact ionization. Fig. 11 also shows that Al ions, forming an approximately 1:1 ratio with Ca ion abundances, are underrepresented in the spectra in comparison to Ca ions, presumably due to their tendency to form anionic species or to remain in molecular ions. It is therefore highly advantageous to use dual mode switching (or simultaneous) spectrometers in space,

allowing the main metal components of minerals to be identified with high accuracy in the positive mode and many oxide components to be identified in the negative mode.

The use of laboratory mineral dust particles as analogues for cosmic dust produces a number of unique challenges, as well as advantages. Organic species, introduced either as part of a conductive coating or via contamination of the impact target, introduce many spurious peaks into hypervelocity impact ionisation spectra. By examining the appearance and amplitudes of peaks within the spectra generated by impact ionisation of anorthite dust grains at different impact velocities we have shown that it is possible to identify features due to the mineral.

Large numbers of Na and K ions are present in the spectra, and thus the impact plasma, due to surface contamination of the mineral particle and the target. Despite this there are no signs of NaX^+ or KX^+ ions. This is consistent with target-projectile ions only forming in appreciable amounts with the bulk target and projectile materials.

There are no high amplitude signals from the coating metal ions, although the metal is definitely present on the accelerated particles. As an example, a spherical anorthite particle with a 5 nm thick, complete Pt coating, accelerated to 10 km s^{-1}, would have a core grain radius of 0.173 μm, compared with a grain radius of 0.3 μm for an uncoated particle of the same mass. The Pt coating will therefore contribute 7.5% of the ions in the plasma, assuming complete particle breakup and ionization. The reduced Pt signal is probably due to three factors: the Pt ions are divided between several isotopes, reducing the amplitude of the peaks, the metal coating may not be being fully ionised and the high electron affinity of Pt will be discouraging the production and survival of Pt cations within the plasma.

Similarly, although there are obviously features due to organic species present in the spectra, there are no strong spectral peaks at masses which would be expected from electron ionisation spectra of MPTMS[2]. This implies that the coating of MPTMS is indeed close to being a molecular monolayer.

Although many of the features in the spectra have not been unambiguously identified as due to a single compound, correlation analysis of impact ionisation spectra of different minerals which have been coated in the same way will help determine which minor features are due to the particle coating and contamination and which are due to the bulk mineral. Suggested species identifications from this data set are shown in Table 4.

Of particular interest are the high mass species identified in the correlation analysis as being of mineral origin. These, at masses 96, 99, 100, 112, 113, 117, 155 and possibly 163 (Ca_2O/$CaSi_2$/CaAlSiH, $CaAlO_2$, $CaSiO_2$, $(CaO)_2$, $(CaO)_2H$, $CaSiO_3H$, Ca_2SiO_3/$Ca_2Si_3O_2$ and possibly $Al_2Si_2O_5$), provide a fingerprint of the mineral, in this case strongly indicative of anorthite. Experiments by *Tsugoshi et al.* [1991] found similar diagnostic features for different families of silicates using Laser Microprobe Mass Spectrometry (LMMS). Impact experiments using the same coating, acceleration methods (with varied acceleration voltages) and detector are currently underway to investigate whether similarly diagnostic features exist for pyrrhotite, orthopyroxene, olivine and silica.

Results presented here, particularly concerning the formation of diagnostic anions in the impact plasma of mineral particles, and the importance of simultaneously measuring the impact velocity and composition of dust grains, are relevant to the development of the next generation of dust detectors. These detectors (e.g. active dust detectors and novel

instruments for use in the Jovian system [*Postberg et al.*, 2011b; *Grün et al.*, 2012; *Kempf et al.*, 2012]) should be dual-mode instruments capable of generating both anion and cation mass spectra, use a target material which has an easily identifiable isotope pattern, and be equipped with dust trajectory sensors that measure the impact velocity of impinging dust. Instruments with these characteristics will offer the best opportunity for the accurate determination of particle compositions and sources.

Acknowledgments. We thank Sebastian Bugiel for his invaluable assistance in running the accelerator. JKH, SS and SFG acknowledge the financial support of the Science and Technology Facilities Council. JKH and ZS acknowledge the funding of NASA. The authors thank E. Grün and an anonymous referee for their extremely helpful comments and discussion.

References

Aléon, J., A. N. Krot, and K. D. McKeegan (2002), Calcium-aluminum-rich inclusions and amoeboid olivine aggregates from the CR carbonaceous chondrites, *Meteoritics and Planetary Science*, *37*, 1729–1755, doi:10.1111/j.1945-5100.2002.tb01160.x.

Alikhanov, S. G. (1957), A new impulse technique for ion mass measurements, *Sov. Phys.-JETP*, *4*, 452–453.

Altobelli, N., E. Grün, and M. Landgraf (2006), A new look into the Helios dust experiment data: presence of interstellar dust inside the Earth's orbit, A&A, *448*, 243–252, doi:10.1051/0004-6361:20053909.

Austin, D. E., R. L. Grimm, H. L. K. Manning, C. L. Bailey, J. E. Farnsworth, T. J. Ahrens, and J. L. Beauchamp (2003), Hypervelocity microparticle impact studies using

a novel cosmic dust mass spectrometer, *Journal of Geophysical Research (Planets)*, *108*, 5038, doi:10.1029/2002JE001947.

Bruynseels, F. J., and R. E. Van Grieken (1983), Molecular ion distributions in laser microprobe mass spectrometry of calcium oxide and calcium salts, *Spectrochimica Acta Part B: Atomic Spectroscopy*, *38*(5-6), 853–858.

Burchell, M. J., M. J. Cole, J. A. M. McDonnell, and J. C. Zarnecki (1999a), Hypervelocity impact studies using the 2 MV Van de Graaff accelerator and two-stage light gas gun of the University of Kent at Canterbury, *Measurement Science and Technology*, *10*, 41–50, doi:10.1088/0957-0233/10/1/011.

Burchell, M. J., M. J. Cole, S. F. Lascelles, M. A. Khan, C. Barthet, S. A. Wilson, D. B. Cairns, and S. P. Armes (1999b), Acceleration of conducting polymer-coated latex particles as projectiles in hypervelocity impact experiments, *Journal of Physics D Applied Physics*, *32*, 1719–1728, doi:10.1088/0022-3727/32/14/325.

Burchell, M. J., M. J. Willis, S. P. Armes, M. A. Khan, M. J. Percy, and C. Perruchot (2002), Impact ionization experiments with low density conducting polymer-based micro-projectiles as analogues of solar system dusts, Planet. Space Sci., *50*, 1025–1035, doi:10.1016/S0032-0633(02)00071-5.

Chen, M., J. Falkner, W.-H. Guo, J.-Y. Zhang, C. Sayes, and V. L. Colvin (2005), Synthesis and self-organization of soluble monodisperse palladium nanoclusters, *Journal of Colloid and Interface Science*, *287*(1), 146 – 151, doi:10.1016/j.jcis.2005.02.003.

Christoffersen, R., and P. R. Buseck (1986), Refractory minerals in interplanetary dust, *Science*, *234*, 590–592, doi:10.1126/science.234.4776.590.

Ciesla, F. J. (2010), The distributions and ages of refractory objects in the solar nebula, Icarus, *208*, 455–467, doi:10.1016/j.icarus.2010.02.010.

Demidova, S. I., M. A. Nazarov, M. Anand, and L. A. Taylor (2003), Lunar regolith breccia Dhofar 287B: A record of lunar volcanism, *Meteoritics and Planetary Science*, *38*, 501–514, doi:10.1111/j.1945-5100.2003.tb00023.x.

Dietzel, H., G. Eichhorn, H. Fechtig, E. Grun, H.-J. Hoffmann, and J. Kissel (1973), The HEOS 2 and HELIOS micrometeoroid experiments, *Journal of Physics E Scientific Instruments*, *6*, 209–217, doi:10.1088/0022-3735/6/3/008.

Dowty, E., M. Prinz, and K. Keil (1974), Ferroan anorthosite - A widespread and distinctive lunar rock type, *Earth and Planetary Science Letters*, *24*, 15–25, doi:10.1016/0012-821X(74)90003-X.

Erel, E., F. Aubriet, G. Finqueneisel, and J.-F. Muller (2003), Capabilities of laser ablation mass spectrometry in the differentiation of natural and artificial opal gemstones, *Analytical Chemistry*, *75*(23), 6422–6429, doi:10.1021/ac034576t.

Fujii, S., S. P. Armes, R. Jeans, R. Devonshire, S. Warren, S. L. McArthur, M. J. Burchell, F. Postberg, and R. Srama (2006), Synthesis and characterization of polypyrrole-coated sulfur-rich latex particles: New synthetic mimics for sulfur-based micrometeorites, *Chemistry of Materials*, *18*(11), 2758–2765.

Gallavardin, S., U. Lohmann, and D. Cziczo (2008), Analysis and differentiation of mineral dust by single particle laser mass spectrometry, *International Journal of Mass Spectrometry*, *274*(1-3), 56–63.

Goldsworthy, B. J., et al. (2002), Laboratory calibration of the cassini cosmic dust analyser (CDA) using new, low density projectiles, *Advances in Space Research*, *29*, 1139–1144,

doi:10.1016/S0273-1177(02)00129-1.

Goldsworthy, B. J., et al. (2003), Time of flight mass spectra of ions in plasmas produced by hypervelocity impacts of organic and mineralogical microparticles on a cosmic dust analyser, A&A, *409*, 1151–1167, doi:10.1051/0004-6361:20031087.

Greshake, A., P. Hoppe, and A. Bischoff (1996), Mineralogy, chemistry, and oxygen isotopes of refractory inclusions from stratospheric interplanetary dust particles and micrometeorites, *Meteoritics and Planetary Science*, *31*, 739–748.

Grossman, L. (2010), Vapor-condensed phase processes in the early solar system, *Meteoritics and Planetary Science*, *45*, 7–20, doi:10.1111/j.1945-5100.2009.01010.x.

Grossman, L., and I. M. Steele (1976), Amoeboid olivine aggregates in the Allende meteorite, Geochim. Cosmochim. Acta, *40*, 149–155, doi:10.1016/0016-7037(76)90172-1.

Grün, E., N. Pailer, H. Fechtig, and J. Kissel (1980), Orbital and physical characteristics of micrometeoroids in the inner solar system as observed by HELIOS 1, *Planet. Space Sci.*, *28*, 333–349, doi:10.1016/0032-0633(80)90022-7.

Grün, E., et al. (2012), Active Cosmic Dust Collector, Planet. Space Sci., *60*, 261–273, doi:10.1016/j.pss.2011.09.006.

Hargraves, R. B., and L. S. Hollister (1972), Mineralogic and Petrologic Study of Lunar Anorthosite Slide 15415,18, *Science*, *175*, 430–432, doi:10.1126/science.175.4020.430.

Hillier, J. K., et al. (2007a), Interplanetary dust detected by the Cassini CDA Chemical Analyser, Icarus, *190*, 643–654, doi:10.1016/j.icarus.2007.03.024.

Hillier, J. K., et al. (2007b), The composition of Saturn's E ring, MNRAS, *377*, 1588–1596, doi:10.1111/j.1365-2966.2007.11710.x.

Hillier, J. K., S. Sestak, S. F. Green, F. Postberg, R. Srama, and M. Trieloff (2009), The production of platinum-coated silicate nanoparticle aggregates for use in hypervelocity impact experiments, Planet. Space Sci., *57*, 2081–2086, doi:10.1016/j.pss.2009.09.019.

Höfer, C. (2010), Preparation and analysis of analogue material for extraterrestrial dust, Bachelor Thesis, Universität Heidelberg, Germany.

Hornung, K., and J. Kissel (1994), On shock wave impact ionization of dust particles, A&A, *291*, 324–336.

Hornung, K., Y. G. Malama, and K. Thoma (1996), Modeling of the very high velocity impact process with respect to in-situ ionization measurements, *Advances in Space Research*, *17*, 77–86, doi:10.1016/0273-1177(95)00762-4.

Ishii, H. A., J. P. Bradley, Z. R. Dai, M. Chi, A. T. Kearsley, M. J. Burchell, N. D. Browning, and F. Molster (2008), Comparison of Comet 81P/Wild 2 Dust with Interplanetary Dust from Comets, *Science*, *319*, 447–, doi:10.1126/science.1150683.

Jeong, S., K. J. Fisher, R. F. Howe, and G. D. Willett (1995), Laser ablation fourier transform mass spectrometric study of zeolites, *Microporous Materials*, *4*(6), 467–473.

Kempf, S., et al. (2005), Composition of Saturnian Stream Particles, *Science*, *307*, 1274–1276, doi:10.1126/science.1106218.

Kempf, S., et al. (2012), Linear high resolution dust mass spectrometer for a mission to the Galilean satellites, Planet. Space Sci., *65*, 10–20, doi:10.1016/j.pss.2011.12.019.

Kissel, J., and F. R. Krueger (1987a), The Organic Component in Dust from Comet Halley as Measured by the PUMA Mass Spectrometer on Board VEGA 1, *Nature*, *326*, 755–760, doi:10.1038/326755a0.

Kissel, J., and F. R. Krueger (1987b), Ion formation by impact of fast dust particles and comparison with related techniques, *Applied Physics A: Materials Science & Processing*, *42*, 69–85, doi:10.1007/BF00618161.

Kissel, J., and F. R. Krueger (2001), Time-of-flight mass spectrometric analysis of ion formation in hypervelocity impact of organic polymer microspheres: Comparison with secondary ion mass spectrometry, 252cf mass spectrometry and laser mass spectrometry, *Rapid Communications in Mass Spectrometry*, *15*(18), 1713–1718.

Kissel, J., et al. (1986a), Composition of comet Halley dust particles from Giotto observations, Nature, *321*, 336–337, doi:10.1038/321336a0.

Kissel, J., et al. (1986b), Composition of comet Halley dust particles from VEGA observations, Nature, *321*, 280–282, doi:10.1038/321280a0.

Kissel, J., et al. (2003), Cometary and Interstellar Dust Analyzer for comet Wild 2, *Journal of Geophysical Research (Planets)*, *108*, 8114, doi:10.1029/2003JE002091.

Kissel, J., F. R. Krueger, J. Silén, and B. C. Clark (2004), The Cometary and Interstellar Dust Analyzer at Comet 81P/Wild 2, *Science*, *304*, 1774–1776, doi:10.1126/science.1098836.

Kissel, J., et al. (2007), Cosima-High Resolution Time-of-Flight Secondary Ion Mass Spectrometer for the Analysis of Cometary Dust Particles onboard Rosetta, Space Sci. Rev., *128*, 823–867, doi:10.1007/s11214-006-9083-0.

Krot, A. N., and K. Keil (2002), Anorthite-rich chondrules in CR and CH carbonaceous chondrites: Genetic link between Ca,Al-rich inclusions and ferromagnesian chondrules, *Meteoritics and Planetary Science*, *37*, 91–111, doi:10.1111/j.1945-5100.2002.tb00797.x.

Langevin, Y., J. Kissel, J.-L. Bertaux, and E. Chassefiere (1987), First statistical analysis of 5000 mass spectra of cometary grains obtained by PUMA 1 (Vega 1) and PIA (Giotto) impact ionization mass spectrometers in the compressed modes, A&A, *187*, 761–766.

Lee, Y.-G., C. Oh, J.-H. Park, S.-M. Koo, and S.-G. Oh (2007), Preparation of Platinum and Palladium Nanotubes Using MPTMS-Functionalized Silica Spheroids as Templates, *Journal of Industrial and Engineering Chemistry*, *13*(2), 319 – 324.

Lucey, P. G. (2004), Mineral maps of the Moon, Geophys. Res. Lett., *31*, L08701, doi: 10.1029/2003GL019406.

Mamyrin, B. A., V. I. Karataev, D. V. Shmikk, and V. A. Zagulin (1973), The mass-reflectron, a new nonmagnetic time-of-flight mass spectrometer with high resolution, *Soviet Journal of Experimental and Theoretical Physics*, *37*, 45.

Matsuura, M., et al. (2004), Polycyclic aromatic hydrocarbons and crystalline silicates in the bipolar post-asymptotic giant branch star iras 162794757, *The Astrophysical Journal*, *604*(2), 791.

McDonnell, J. A. M., E. D. Aguti, and M. J. Willis (2001), Pre-contact Microdischarge from Charged Particulates, in *Spacecraft Charging Technology*, *ESA Special Publication*, vol. 476, edited by R. A. Harris, pp. 423–428.

Mellado, E. M., K. Hornung, R. Srama, J. Kissel, S. P. Armes, and S. Fujii (2011), Mass spectrometry of impact fragmented polymers: The role of target properties, *International Journal of Impact Engineering*, *38*(6), 486–494.

Mocker, A., et al. (2011), A 2 MV Van de Graaff accelerator as a tool for planetary and impact physics research, *Review of Scientific Instruments*, *82*(9), 095,111, doi: 10.1063/1.3637461.

Ohtake, M., et al. (2009), The global distribution of pure anorthosite on the Moon, Nature, *461*, 236–240, doi:10.1038/nature08317.

Postberg, F., S. Kempf, R. Srama, S. F. Green, J. K. Hillier, N. McBride, and E. Grün (2006), Composition of jovian dust stream particles, Icarus, *183*, 122–134, doi:10.1016/j.icarus.2006.02.001.

Postberg, F., S. Kempf, J. K. Hillier, R. Srama, S. F. Green, N. McBride, and E. Grün (2008), The E-ring in the vicinity of Enceladus. II. Probing the moon's interior-The composition of E-ring particles, Icarus, *193*, 438–454, doi:10.1016/j.icarus.2007.09.001.

Postberg, F., S. Kempf, J. Schmidt, N. Brilliantov, A. Beinsen, B. Abel, U. Buck, and R. Srama (2009a), Sodium salts in E-ring ice grains from an ocean below the surface of Enceladus, Nature, *459*, 1098–1101, doi:10.1038/nature08046.

Postberg, F., S. Kempf, D. Rost, T. Stephan, R. Srama, M. Trieloff, A. Mocker, and M. Goerlich (2009b), Discriminating contamination from particle components in spectra of Cassini's dust detector CDA, Planet. Space Sci., *57*, 1359–1374, doi: 10.1016/j.pss.2009.06.027.

Postberg, F., J. Schmidt, J. Hillier, S. Kempf, and R. Srama (2011a), A salt-water reservoir as the source of a compositionally stratified plume on Enceladus, Nature, *474*, 620–622, doi:10.1038/nature10175.

Postberg, F., et al. (2011b), Compositional mapping of planetary moons by mass spectrometry of dust ejecta, Planet. Space Sci., *59*, 1815–1825, doi: 10.1016/j.pss.2011.05.001.

Sasaki, S., and E. Kurahashi (2004), Space weathering on Mercury, *Advances in Space Research*, *33*, 2152–2155, doi:10.1016/S0273-1177(03)00442-3.

Shibata, H., et al. (2001), Microparticle acceleration by a Van de Graaff accelerator and application to space and material sciences, *Radiation Physics and Chemistry*, *60*, 277–282, doi:10.1016/S0969-806X(00)00362-5.

Silva, P. J., R. A. Carlin, and K. A. Prather (2000), Single particle analysis of suspended soil dust from southern california, *Atmospheric Environment*, *34*(11), 1811–1820.

Simon, S. B., et al. (2008), A refractory inclusion returned by Stardust from comet 81P/Wild 2, *Meteoritics and Planetary Science*, *43*, 1861–1877, doi:10.1111/j.1945-5100.2008.tb00648.x.

Sprague, A. L., D. B. Nash, F. C. Witteborn, and D. P. Cruikshank (1997), Mercury's feldspar connection - Mid-IR measurements suggest plagioclase, *Advances in Space Research*, *19*, 1507, doi:10.1016/S0273-1177(97)00363-3.

Srama, R., et al. (2004), The Cassini Cosmic Dust Analyzer, Space Sci. Rev., *114*, 465–518, doi:10.1007/s11214-004-1435-z.

Srama, R., S. Kempf, G. Moragas-Klostermeyer, M. Landgraf, S. Helfert, Z. Sternovsky, M. Rachev, and E. Gruen (2007), Laboratory tests of the Large Area Mass Analyser, *Dust in Planetary Systems*, *643*, 209–212.

Srama, R., et al. (2009), Mass spectrometry of hyper-velocity impacts of organic micrograins, *Rapid Communications in Mass Spectrometry*, *23*(24), 3895–3906, doi:10.1002/rcm.4318.

Stern, S. A., et al. (2011), Ultraviolet Discoveries at Asteroid (21) Lutetia by the Rosetta Alice Ultraviolet Spectrograph, AJ, *141*, 199, doi:10.1088/0004-6256/141/6/199.

Sternovsky, Z., et al. (2007a), The Large Area Mass Analyzer (LAMA) for in situ Chemical Analysis of Interstellar Dust Particles, *Dust in Planetary Systems*, *643*, 205–209.

Sternovsky, Z., et al. (2007b), Large Area Mass Analyzer instrument for the Chemical Analysis of Interstellar Dust Particles, *Rev. Sci. Instrum.*, *78*, 014,501 1–10.

Sternovsky, Z., et al. (2011), Novel instrument for dust astronomy: Dust telescope, in *Aerospace Conference, 2011 IEEE*, pp. 1 –8, doi:10.1109/AERO.2011.5747300.

Struyf, H., L. Van Vaeck, K. Poels, and R. Van Grieken (1998), Fourier transform laser microprobe mass spectrometry for the molecular identification of inorganic compounds, *Journal of the American Society for Mass Spectrometry*, *9*(5), 482–497.

Sullivan, R. C., S. A. Guazzotti, D. A. Sodeman, and K. A. Prather (2007), Direct observations of the atmospheric processing of asian mineral dust, *Atmospheric Chemistry and Physics*, *7*(5), 1213–1236.

Sunshine, J. M., H. C. Connolly, T. J. McCoy, S. J. Bus, and L. M. La Croix (2008), Ancient Asteroids Enriched in Refractory Inclusions, *Science*, *320*, 514–, doi: 10.1126/science.1154340.

Sysoev, A. A., V. P. Ivanov, Y. A. Surkov, V. V. Vysochkin, and T. V. Barinova Komova (1997), Mass spectra formation from charged microparticles, *Nuclear Instruments and Methods in Physics Research B*, *122*, 79–83, doi:10.1016/S0168-583X(96)00460-0.

Taylor, M., and G. E. Brown, Jr. (1979), Structure of mineral glasses–I. The feldspar glasses $NaAlSi_3O_8$, $KAlSi_3O_8$, $CaAl_2Si_2O_8$, Geochim. Cosmochim. Acta, *43*, 61–75, doi: 10.1016/0016-7037(79)90047-4.

Taylor, S., G. F. Herzog, and J. S. Delaney (2007), Crumbs from the crust of Vesta: Achondritic cosmic spherules from the South Pole water well, *Meteoritics and Planetary Science*, *42*, 223–233, doi:10.1111/j.1945-5100.2007.tb00229.x.

Trimborn, A., K. . Hinz, H. Iglseder, M. Greweling, and B. Spengler (1998), Characterisation of mineral dust samples using bipolar on-line laser mass spectrometry, *Journal of Aerosol Science*, *29*(SUPPL.2), S883–S884.

Tsugoshi, T., T. Kikuchi, K. Furuya, Y. Ino, and Y. Hayashi (1991), Structural interpretation on silicate network of various silicate minerals by lmms analysis, *Mikrochimica acta*, *105*(4-6), 125–136.

Warell, J. (2002), Properties of the Hermean Regolith. II. Disk-Resolved Multicolor Photometry and Color Variations of the "Unknown" Hemisphere, Icarus, *156*, 303–317, doi:10.1006/icar.2002.6814.

Warell, J., A. Sprague, R. Kozlowski, D. A. Rothery, N. Lewis, J. Helbert, and E. Cloutis (2010), Constraints on Mercury's surface composition from MESSENGER and ground-based spectroscopy, Icarus, *209*, 138–163, doi:10.1016/j.icarus.2010.04.008.

Wark, D. A. (1987), Plagioclase-rich inclusions in carbonaceous chondrite meteorites - Liquid condensates?, Geochim. Cosmochim. Acta, *51*, 221–242, doi:10.1016/0016-7037(87)90234-1.

Wood, J. A., J. S. Dickey, Jr., U. B. Marvin, and B. N. Powell (1970), Lunar anorthosites and a geophysical model of the moon, *Geochimica et Cosmochimica Acta Supplement*, *1*, 965.

Xu, C., R. . Zhang, L. Zhu, L. Zhao, S. . Qian, Y. . Li, and Y. . Long (1997), The generation mechanism of gaseous [(sio2)nx]- clusters, *Kao Teng Hsueh Hsiao Hua Heush Hsueh Pao/ Chemical Journal of Chinese Universities*, *18*(6), x29–946.

Xu, C., Y. Long, R. Zhang, L. Zhao, S. Qian, and Y. Li (1998), Laser ablation time-of-flight mass spectrometric probing of the surface states of sio2-based porous materials,

Applied Physics A: Materials Science and Processing, *66*(1), 99–102.

Yan, B., R. Wang, F. Gan, and Z. Wang (2010), Minerals mapping of the lunar surface with Clementine UVVIS/NIR data based on spectra unmixing method and Hapke model, Icarus, *208*, 11–19, doi:10.1016/j.icarus.2010.01.030.

Zolensky, M. E., et al. (2006), Mineralogy and Petrology of Comet 81P/Wild 2 Nucleus Samples, *Science*, *314*, 1735–, doi:10.1126/science.1135842.

Figure 1. The measured mass and velocity distribution of the accelerated anorthite particles. Particles for which cation spectra were obtained are marked by triangles, particles for which anion spectra were obtained are marked by crosses. The best fit line was generated after a 1.5σ clip to remove outlying points. Particle masses rather than radii are shown as uncertainties in the Pt coating thickness make estimates of particle radii unreliable.

Figure 2. The measured velocity distributions of the accelerated anorthite particles. Particles for which cation spectra were obtained are shown in light gray, particles for which anion spectra were obtained are shown in dark gray.

Figure 3. The observed scatter in measured peak amplitude for selected elements in the eight spectra co-added for the 10-10.999 km s^{-1} velocity bin.

Figure 4. Sum spectrum of 299 impact ionisation anorthite mass spectra obtained from impacts at velocities of between 0.5 and 32 km s^{-1}. The "tails" present on the larger peaks are artefacts of the plasma production process and are accounted for in all subsequent interpretation of the spectra.

Figure 5. Sum impact ionisation mass spectra of anorthite for velocity bins between zero and five km s^{-1}.

Figure 6. Sum impact ionisation mass spectra of anorthite for velocity bins between five and ten km s^{-1}.

Figure 7. Sum impact ionisation mass spectra of anorthite for velocity bins between ten and fifteen km s^{-1}.

Figure 8. Sum impact ionisation mass spectra of anorthite for velocity bins between fifteen and twenty-two km s^{-1}.

Figure 9. Sum impact ionisation mass spectra of anorthite for velocity bins between twenty-two and thirty-three km s^{-1}.

Figure 10. The fractional difference in the measured abundances of the ^{107}Ag and ^{109}Ag peaks, and the peak amplitudes (a reasonable proxy for total ion numbers), as functions of velocity. Data points linked by lines show the measured abundance of the ^{107}Ag and ^{109}Ag peaks, with amplitudes shown on the right hand ordinate axis. The + symbols show the fractional difference between the isotopic abundances, given by $\frac{^{107}Ag - ^{109}Ag}{^{107}Ag + ^{109}Ag}$

, and measured on the left hand ordinate axis. The horizontal dashed line shows the expected fractional difference in the isotopic abundance for the natural stable isotope abundances (0.51839 and 0.48161 for the 107 and 109 u Ag isotopes respectively). This is therefore $\frac{0.5184 - 0.4816}{1} = 0.0368$.

Figure 11. The abundance of the ^{27}Al peak as a function of the abundance of the ^{40}Ca peak. The fit line, constrained to pass through [0,0], is Ca = 0.79×Al.

Figure 12. The amplitude of the 16 u (oxygen) peak from sum spectra for different impact velocity ranges.

Figure 13. The amplitudes of the Na, K and Ca peaks at different impact velocities.

Figure 14. The trend of the amplitudes of the 28, 29 and 30 u peaks (divided by the sum of their amplitudes) as a function of impact velocity.

Figure 15. The fractional abundance of the 41 u peak, assuming it to be K (41 u/(39 u + 41 u)) as a function of impact velocity.

Figure 16. The amplitudes of the 27 u, 29 u and ^{40}Ca peaks for each sum spectrum at different impact velocities. Ca is still present at statistically significant levels at the highest impact velocity.

Figure 17. The amplitudes of the 54, 55 56, 57 and 58 u peaks at different impact velocities.

Figure 18. The amplitudes of the 64, 65 and 66 u peaks at different impact velocities. The signals are extremely low, with an error range of between 1.8 and 7, depending on the number of spectra contributing to each point, although the appearance of each species is concomitant.

Table 1. Ionization energies, electron affinities and Pauling electronegativities for ions expected in this sample of spectra, together with the most likely origin for the species observed (C: conductive coating, P: mineral particle, T: impact target, X: processing contamination).

Element	Ionisation Energy (kJ mol^{-1})	Electron Affinity (kJ mol^{-1})	Electronegativity	Origin
H	1312	-72.77	2.2	CX
B	800.6	-26.99	2.04	X
C	1086.5	-121.78	2.55	CX
O	1402.3	-7	3.04	PCX
N	1313.9	-141.004	3.44	X
Na	495.8	-52.87	0.93	X
Al	577.5	-41.86	1.61	P
Si	786.5	-134.07	1.9	P
S	999.6	-200.41	2.58	C
Cl	1251.2	-349	3.16	X
K	418.8	-48.38	0.82	X
Ca	589.8	-2.37	1	P
Ag	731	-125.86	1.93	T
Pt	870	-205.04	2.28	C

Table 2. Composition of the Anorthite grains used.

Species	Na	Mg	Al	Si	K	Ca	Fe	O
Absolute Percentage	0.12	0.02	19.63	20.02	0.05	14.01	0.03	46.17

Table 3. The velocity ranges, midpoint masses, midpoint "particle" charges and number of spectra contributing, for the binned cation spectra. Midpoint masses and charges were calculated from the best fit line in Fig. 1 and the relationship between mass, velocity and acceleration voltage..

Velocity Range (km s^{-1})	Midpoint mass (kg)	Midpoint charge (C)	Number of spectra
0 – 0.999	4.18×10^{-13}	3.93×10^{-11}	3
1 – 1.999	1.65×10^{-14}	1.40×10^{-11}	19
2 – 2.999	3.68×10^{-15}	8.64×10^{-12}	25
3 – 3.999	1.37×10^{-15}	6.30×10^{-12}	21
4 – 4.999	6.53×10^{-16}	4.97×10^{-12}	49
5 – 5.999	3.62×10^{-16}	4.11×10^{-12}	32
6 – 6.999	2.21×10^{-16}	3.52×10^{-12}	20
7 – 7.999	1.45×10^{-16}	3.07×10^{-12}	14
8 – 8.999	1.01×10^{-16}	2.73×10^{-12}	14
9 – 9.999	7.25×10^{-17}	2.46×10^{-12}	13
10 – 10.999	5.40×10^{-17}	2.24×10^{-12}	8
11 – 11.999	4.14×10^{-17}	2.06×10^{-12}	8
12 – 12.999	3.24×10^{-17}	1.90×10^{-12}	12
13 – 13.999	2.58×10^{-17}	1.77×10^{-12}	10
14 – 14.999	2.09×10^{-17}	1.65×10^{-12}	11
15 – 16.999	1.57×10^{-17}	1.51×10^{-12}	7
17 – 17.999	1.20×10^{-17}	1.38×10^{-12}	6
18 – 18.999	1.02×10^{-17}	1.31×10^{-12}	5
19 – 19.999	8.75×10^{-18}	1.25×10^{-12}	5
20 – 20.999	7.55×10^{-18}	1.19×10^{-12}	6
21 – 24.999	5.39×10^{-18}	1.07×10^{-12}	7
25 – 32.999	2.72×10^{-18}	8.61×10^{-13}	4

Table 4. Identification of 3σ significant spectral features observed within the sum spectrum shown in Fig. 4. Species marked with * are present below the 3σ limit but indicated by the presence of related isotope(s). Masses are to the nearest Dalton. Mineral indicates possible source species from the anorthite, Other indicates a source from the coating, target or contamination.

Mass	Mineral	Other	Mass	Mineral	Other
1		H	63		$(CH_3)_2SH$, C_5H_3
2		H_2	64		$SHOCH_3$, C_5H_4
3		H_3	65		C_5H_5
6*		Li	66		C_5H_6
7		Li	67	CaAl	C_5H_7
10*		B	69	CaSiH	C_5H_9
11		B	71	AlSiO	C_5H_{11}
12		C	72	CaO_2, AlSiOH	
13		CH	73	CaO_2H	CH_2SiOCH_3
14		CH_2, N	75	AlO_3	$(CH_2)_3SH$, $(CH_3)_2SiOH$
16	O	O, CH_4	77		$CH_2(CH_3)_2SH$, C_6H_5
23		Na	79		C_6H_7
27	Al	C_2H_3	81		C_6H_9
28	Si	C_2H_4, Si	83	AlCaO	C_6H_{11}
29	Si	C_2H_5, CHO, Si	85	CaSiOH	C_6H_{13}
30	Si	C_2H_6?, Si	91		$SHSiOCH_3$
31		OCH_3	96	Ca_2O, CaAlSiH, $CaSi_2$	
32		S	99	$CaAlO_2$	C_7H_{15}
33		SH	100	$CaSiO_2$	
34		S, SH_2	107		Ag
35		Cl	109		Ag
37*		Cl	117	$CaSiO_3H$	
39		K, C_3H_3	147	AgCa	AgCa
40	Ca	C_3H_4	149	AgCa	AgCa
41		K, C_3H_5	151*	AgSiO, AgAlOH	AgSiO, AgAlOH
43	AlO	C_3H_7	153	AgSiO, AgAlOH	AgSiO, AgAlOH
44	AlOH , SiO, Ca	CO_2	155	Ca_2AlO_3	
45	SiO, SiOH	CO_2H, CH_2OCH_3	163*	AgCaO, $AgSi_2$, AgAlSiH	AgCaO, $AgSi_2$, AgAlSiH
48		$SHCH_3$	165	AgCaO, $AgSi_2$, AgAlSiH	AgCaO, $AgSi_2$, AgAlSiH
53		C_4H_3	194		Pt
55	AlSi	C_4H_7	195		Pt
56	CaO, Si_2, AlSiH	C_4H_8	196		Pt
57	CaOH, $AlSiH_2$	C_4H_9	198		Pt
58		C_2H_2S	214		Ag
59	AlO_2	$SiOCH_3$	216		Ag
61		$(CH_2)_2SH$	218		Ag

Table 5. Velocity thresholds for the appearance and disappearance of different species in the Anorthite spectra. As the appearance of species at velocities as low as 0.5 km s^{-1} is unusual, the next highest velocities at which particular species appear have also been shown. Velocities of >29 km s^{-1} indicate that the species was still present in the highest velocity sum spectrum presented here, not that this was the velocity at which the species was no longer detectable.

Mass (u)	V_{appear}	$V_{appear>0.5}$	$V_{disappear}$	Mass (u)	V_{appear}	$V_{appear>0.5}$	$V_{disappear}$
1	0.5	1.5	>29	58	1.5		10.5
2	0.5	7.5	>29	59	1.5		8.5
3	11.5		16	61	2.5		8.5
7	2.5		12.5	63	2.5		16
10	14.5		20.5	64	2.5		16
11	7.5		29	65	1.5		16
12	0.5	1.5	>29	66	2.5		16
13	0.5	7.5	>29	67	1.5		10.5
14	0.5	9.5	>29	69	1.5		5.5
16	0.5	9.5	>29	71	1.5		9.5
23	0.5	1.5	20.5	72	1.5		10.5
27	1.5		>29	73	0.5	1.5	18.5
28	2.5		>29	75	1.5		16
29	1.5		20.5	77	1.5		10.5
30	2.5		14.5	79	2.5		5.5
31	2.5		10.5	81	1.5		5.5
32	4.5		>29	83	1.5		20.5
33	3.5		10.5	85	1.5		10.5
34	3.5		10.5	91	1.5		4.5
35	5.5		>29	96	3.5		16
39	0.5	1.5	29	99	2.5		16
40	0.5	1.5	29	100	3.5		13.5
41	1.5		20.5	107	0.5	1.5	29
43	0.5	1.5	20.5	109	0.5	1.5	29
44	1.5		20.5	117	2.5		9.5
45	0.5	1.5	18.5	147	0.5	3.5	14.5
48	0.5	1.5	16	149	7.5		14.5
53	1.5		12.5	155	0.5	5.5	16
54	4.5		16	194-198	7.5		13.5
55	1.5		16	214	3.5		29
56	0.5	1.5	20.5	216	3.5		29
57	1.5		20.5	218	3.5		29

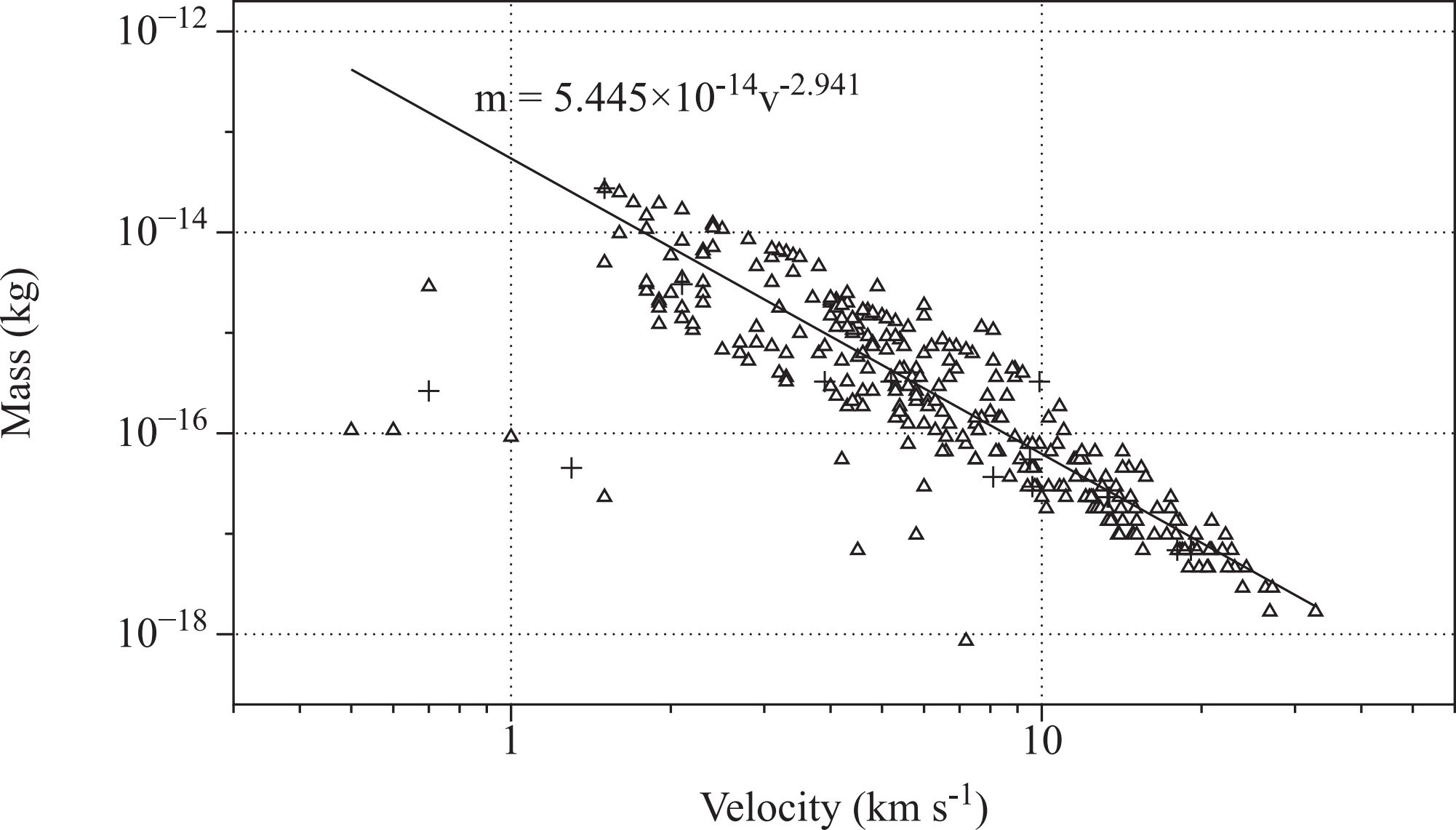
$m = 5.445\times10^{-14}v^{-2.941}$
10^{-12}
10^{-14}
10^{-16}
10^{-18}
Mass (kg)
1
10
Velocity (km s^{-1})

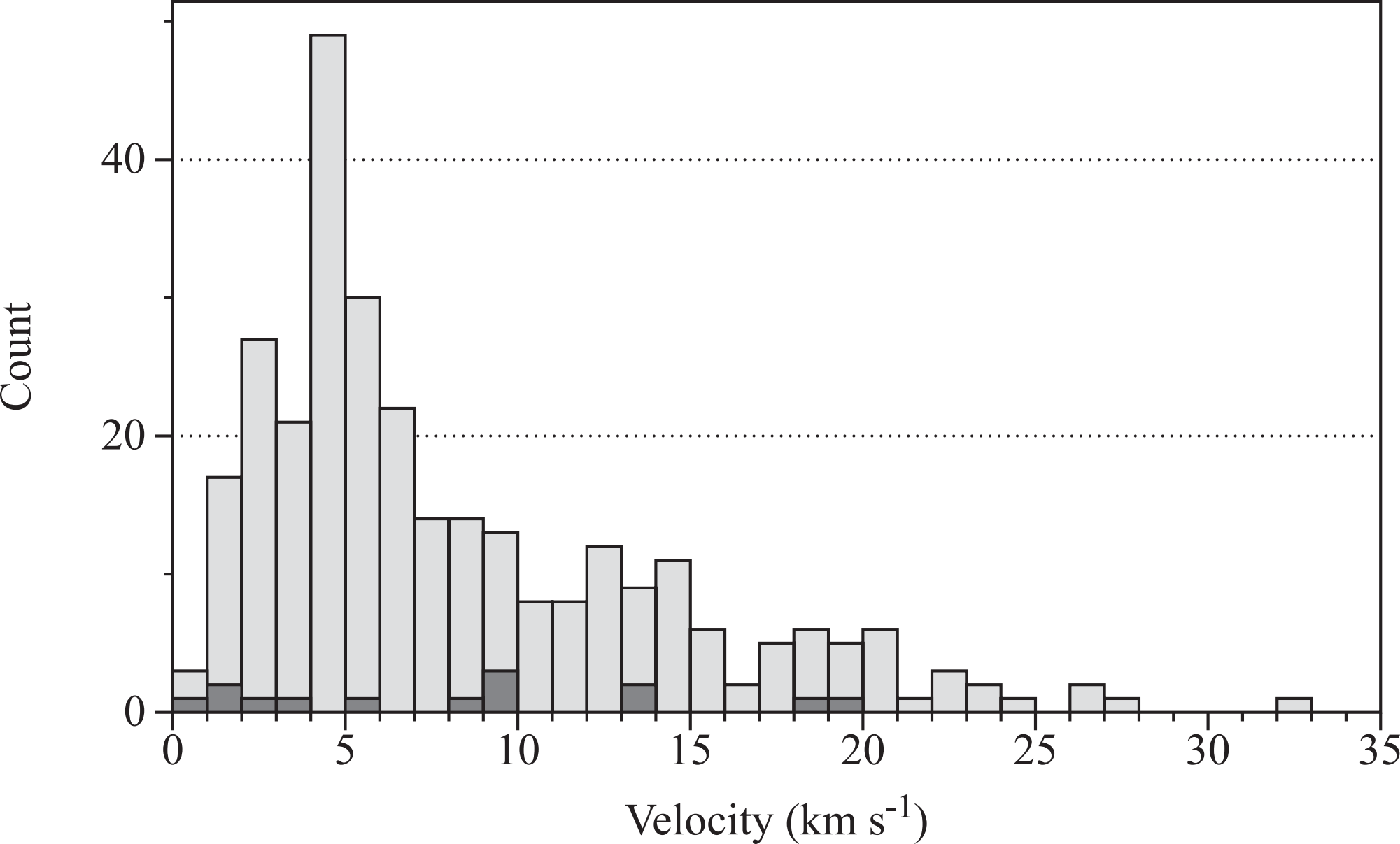
Count
0
20
40
0
5
10
15
20
25
30
35
Velocity (km s-1)

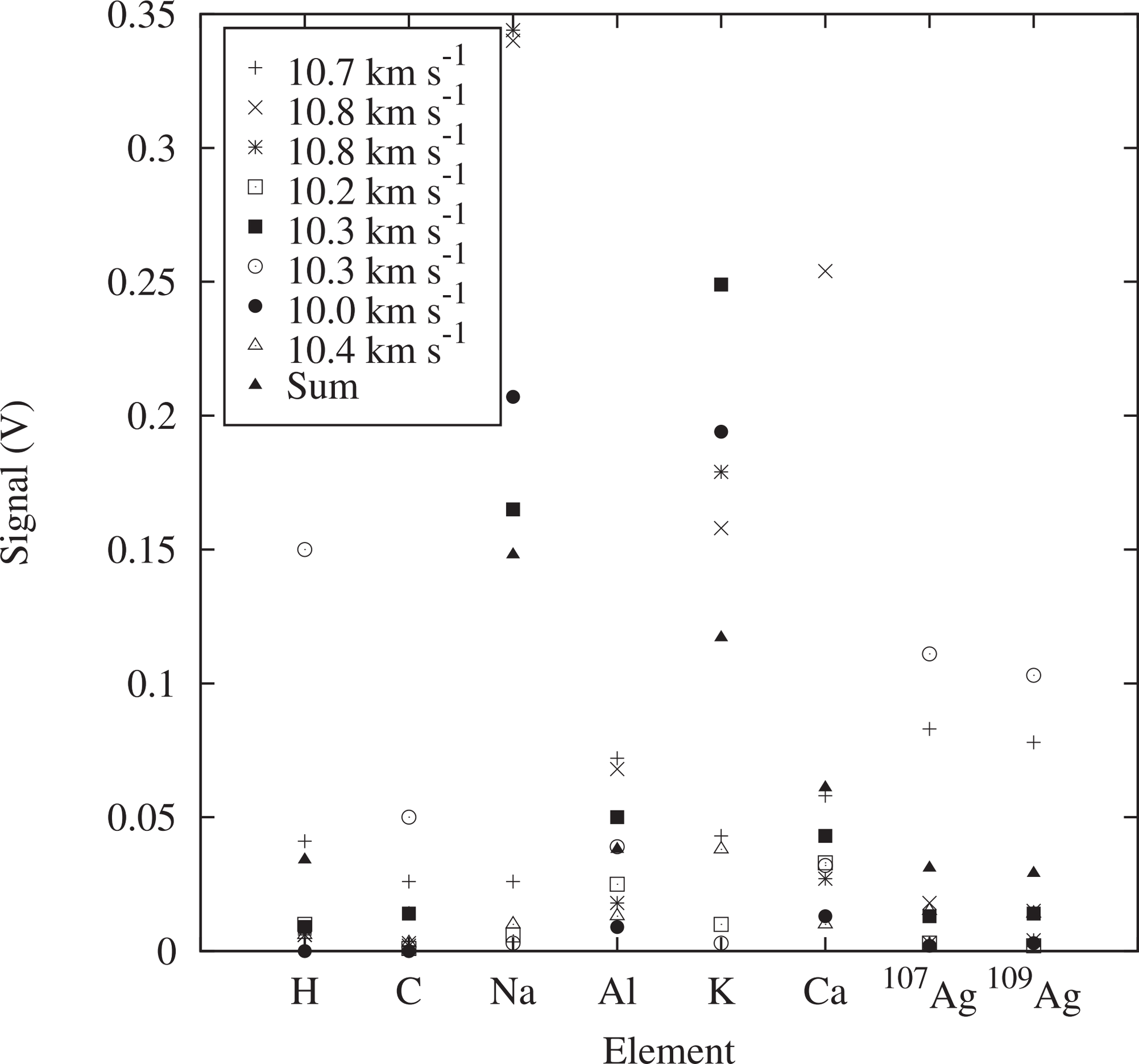
0.35
0.3
0.25
0.2
0.15
0.1
0.05
0
Signal (V)
10.7 km s-1
10.8 km s-1
10.8 km s-1
10.2 km s-1
10.3 km s-1
10.3 km s-1
10.0 km s-1
10.4 km s-1
Sum
H
C
Na
Al
K
Ca
107Ag
109Ag
Element

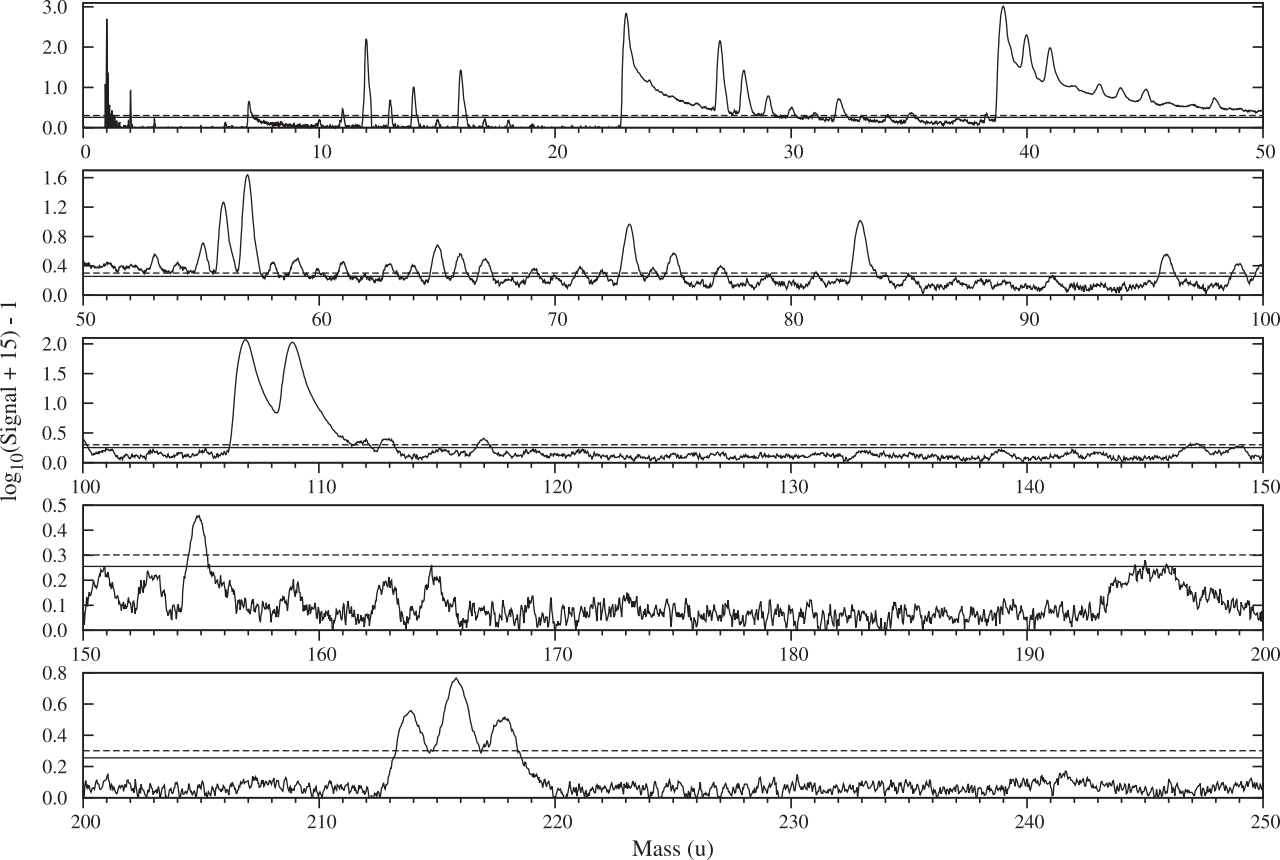
log10(Signal + 15) - 1
Mass (u)

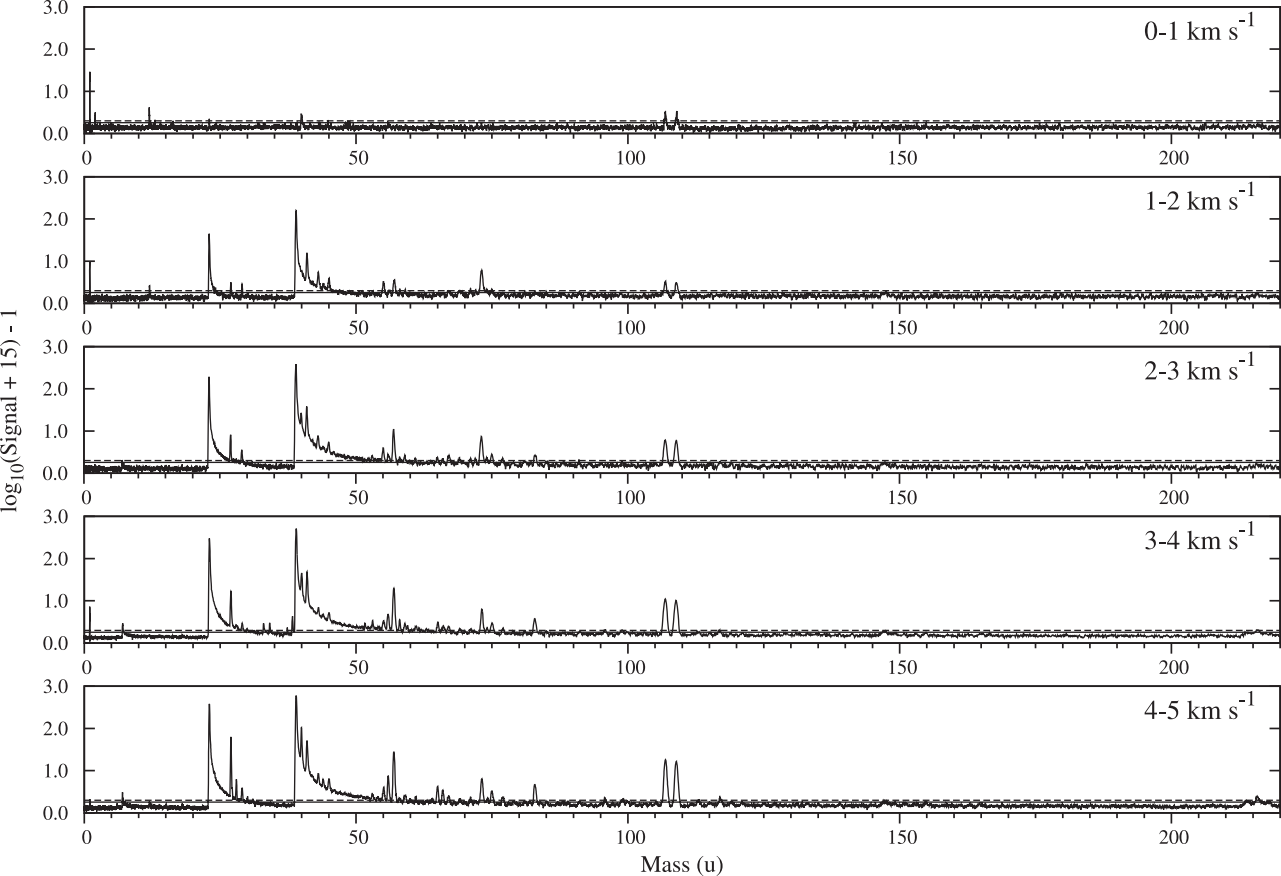
0-1 km s-1
1-2 km s-1
2-3 km s-1
3-4 km s-1
4-5 km s-1
log10(Signal + 15) - 1
Mass (u)
0.0
1.0
2.0
3.0
0
50
100
150
200

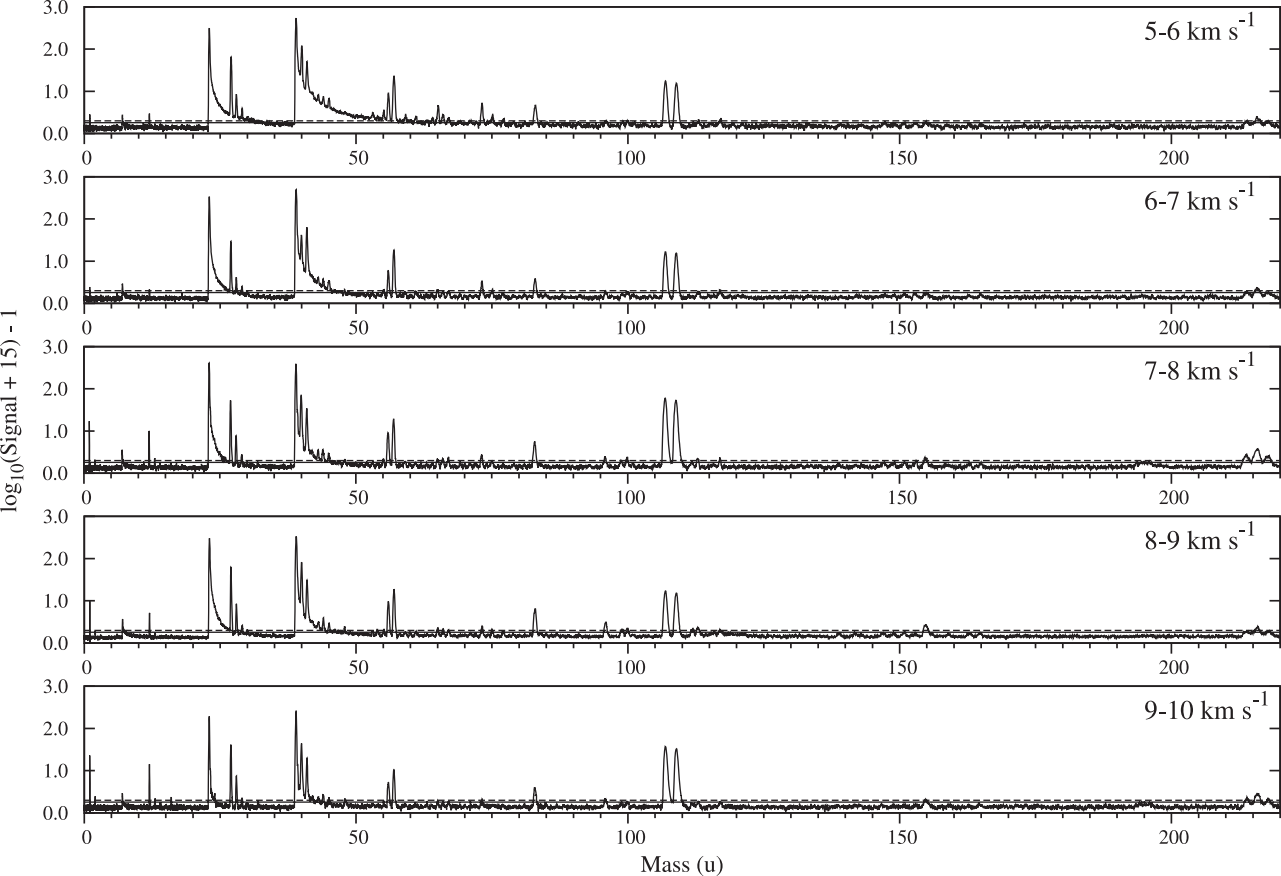
5-6 km s-1
6-7 km s-1
7-8 km s-1
8-9 km s-1
9-10 km s-1
log10(Signal + 15) - 1
Mass (u)
0.0
1.0
2.0
3.0
0
50
100
150
200

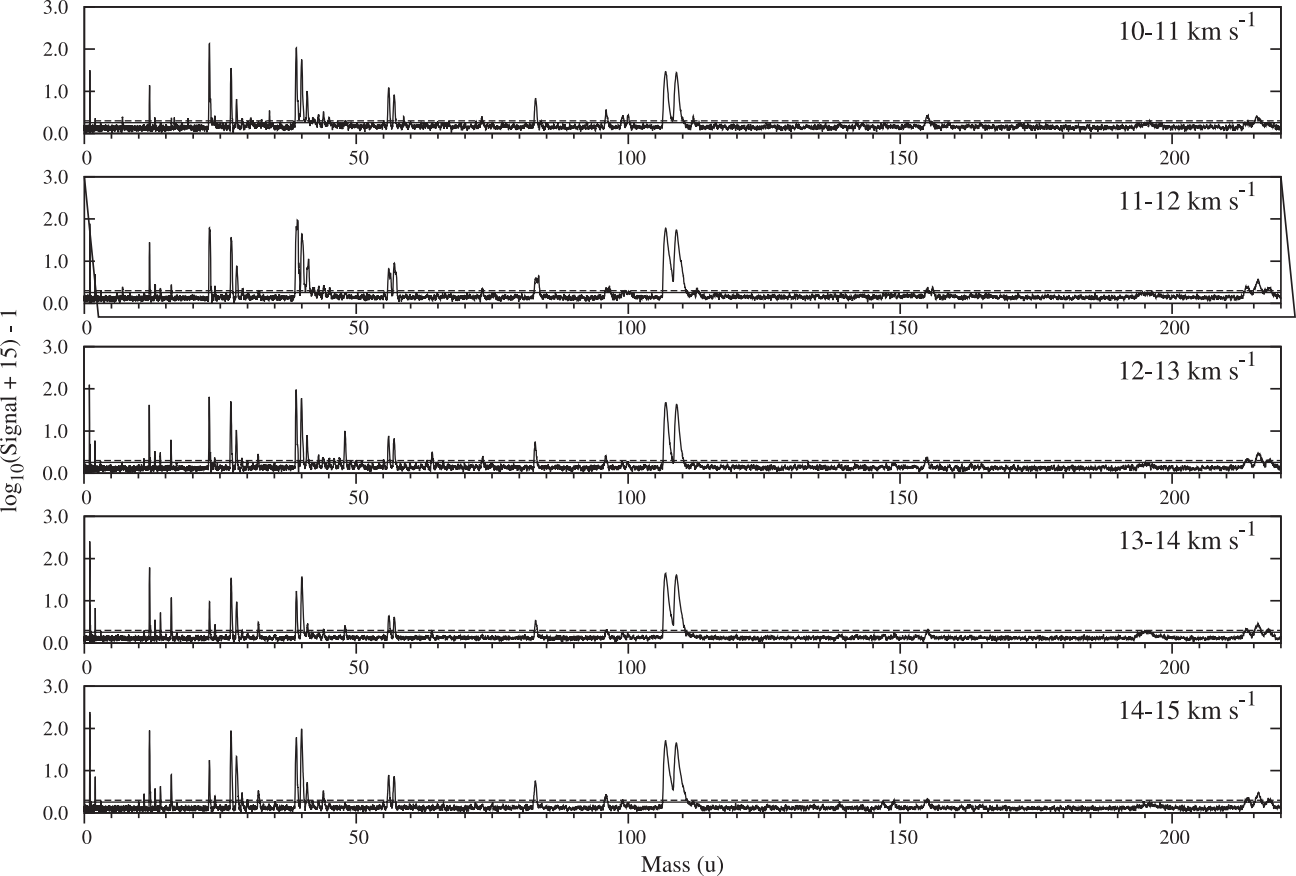
10-11 km s-1
11-12 km s-1
12-13 km s-1
13-14 km s-1
14-15 km s-1
log10(Signal + 15) - 1
Mass (u)
0.0
1.0
2.0
3.0
0
50
100
150
200

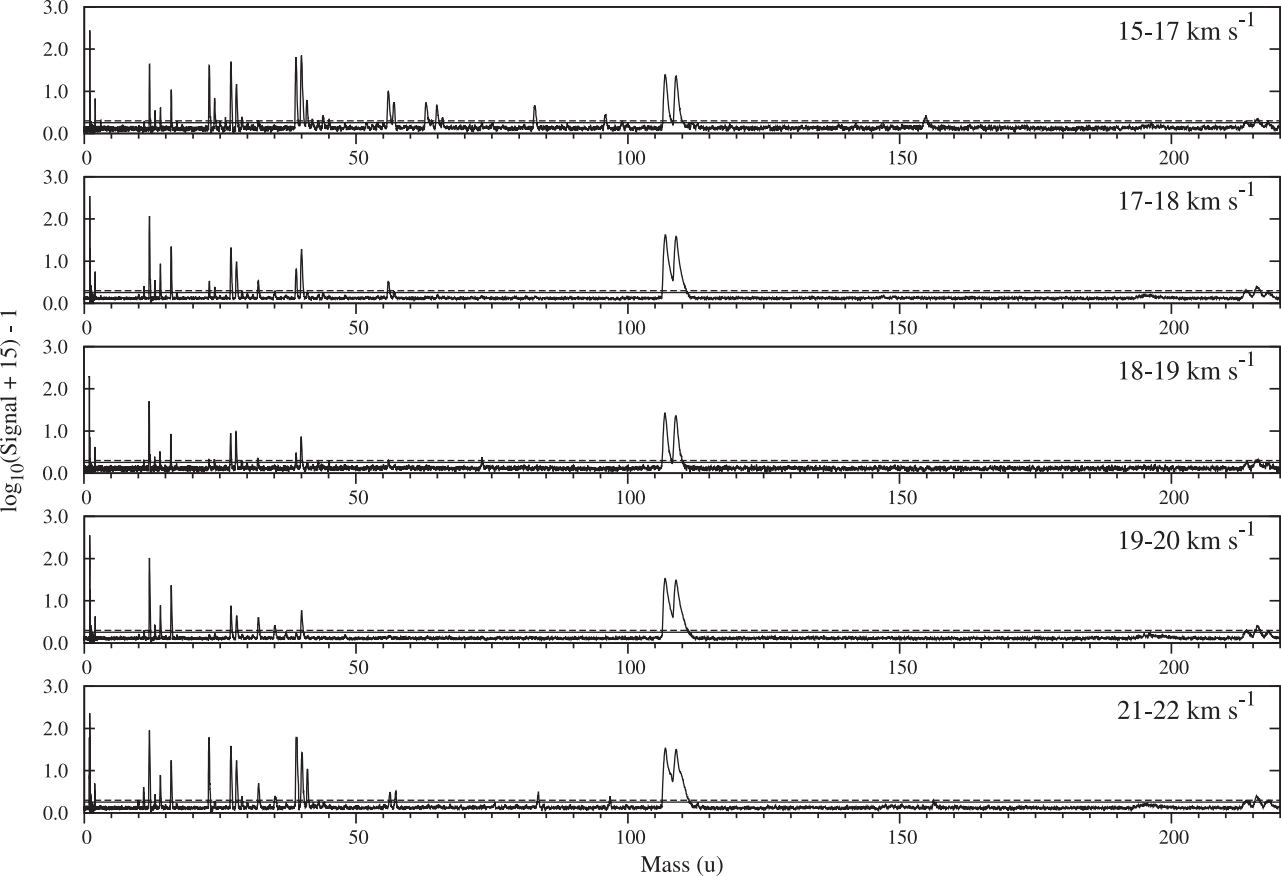
15-17 km s-1
17-18 km s-1
18-19 km s-1
19-20 km s-1
21-22 km s-1
log10(Signal + 15) - 1
Mass (u)
0.0
1.0
2.0
3.0
0
50
100
150
200

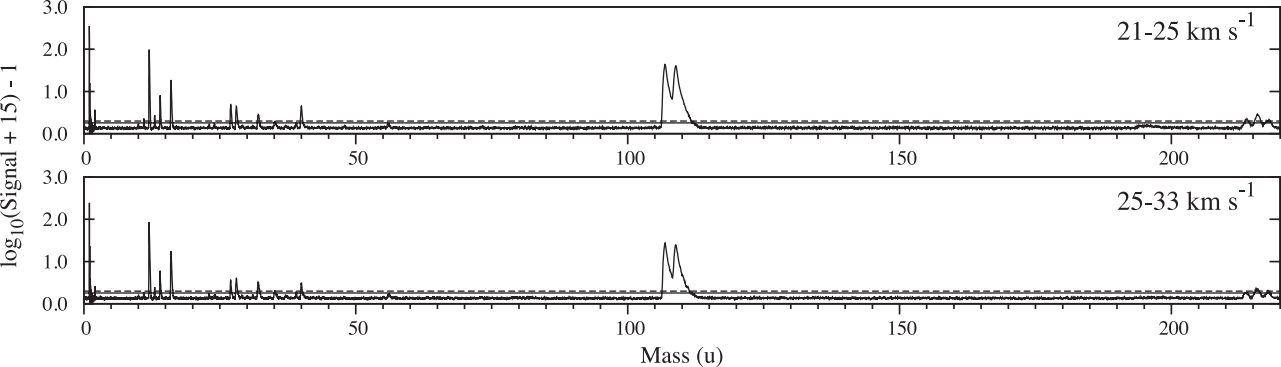
21-25 km s-1
25-33 km s-1
log10(Signal + 15) - 1
3.0
2.0
1.0
0.0
0
50
100
150
200
Mass (u)

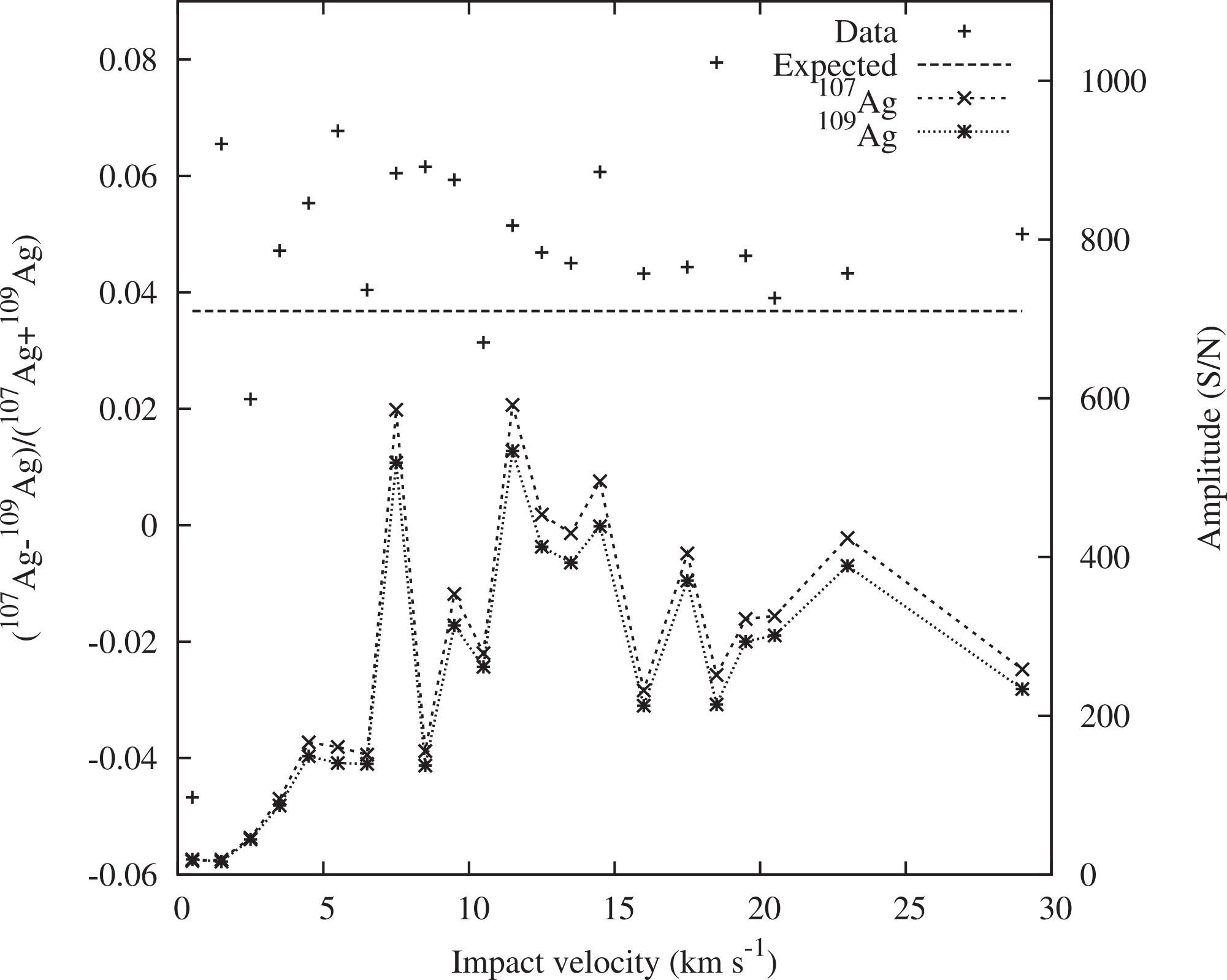
Data
Expected
107Ag
109Ag
0.08
0.06
0.04
0.02
0
-0.02
-0.04
-0.06
1000
800
600
400
200
0
0
5
10
15
20
25
30
(107Ag-109Ag)/(107Ag+109Ag)
Amplitude (S/N)
Impact velocity (km s-1)

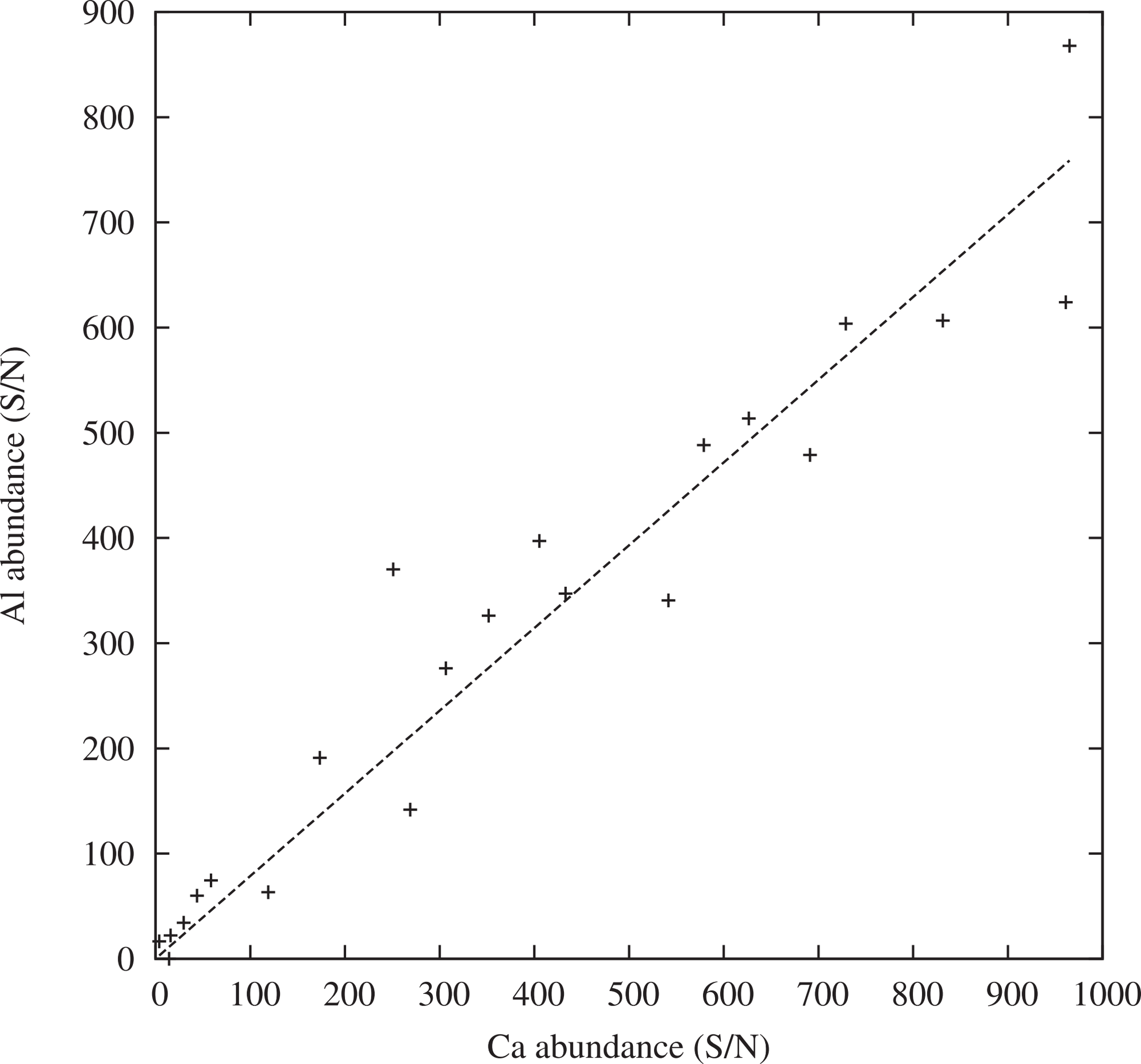
Al abundance (S/N)
Ca abundance (S/N)
0
100
200
300
400
500
600
700
800
900
1000

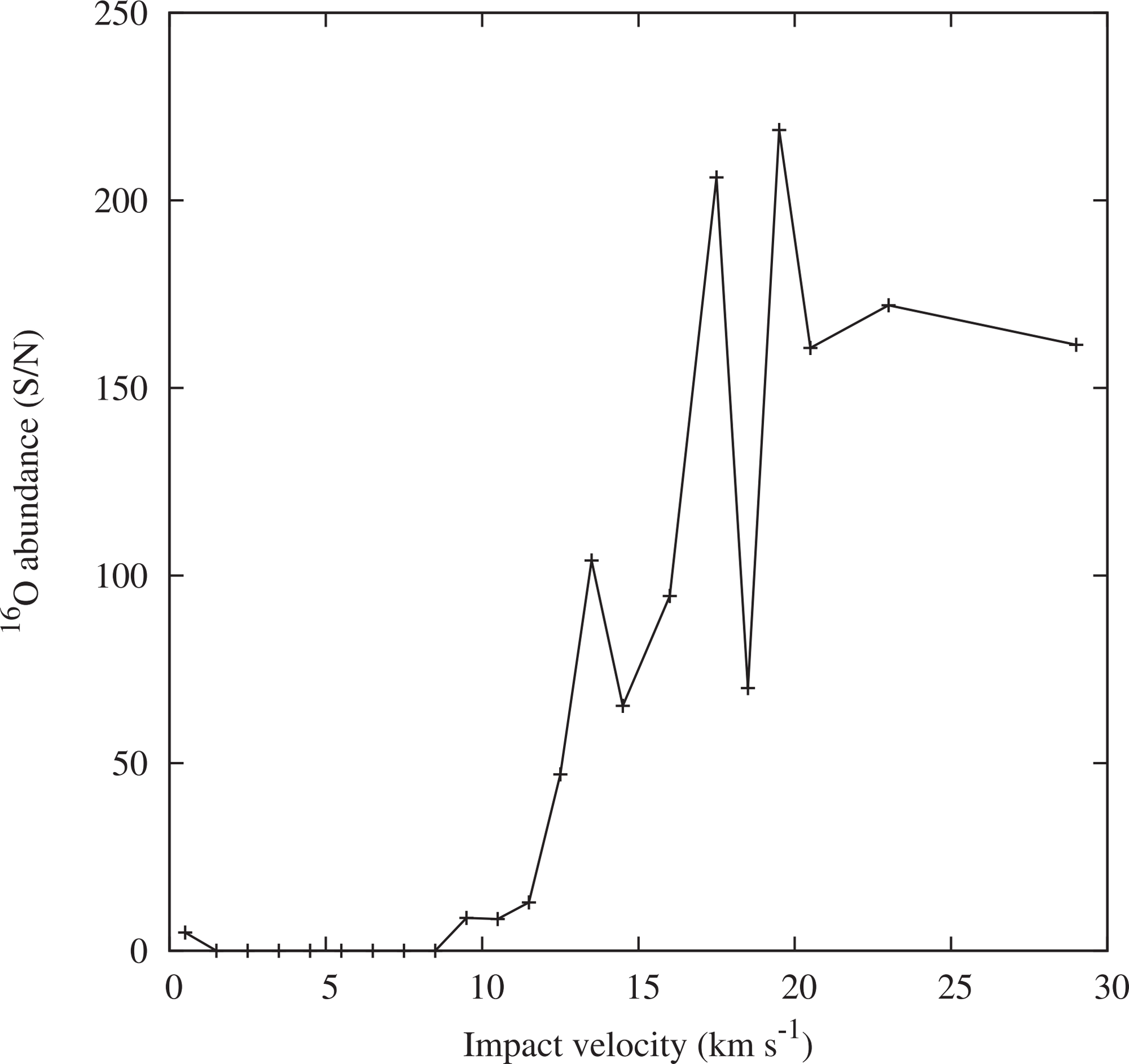
250
200
150
100
50
0
0
5
10
15
20
25
30
^{16}O abundance (S/N)
Impact velocity (km s^{-1})

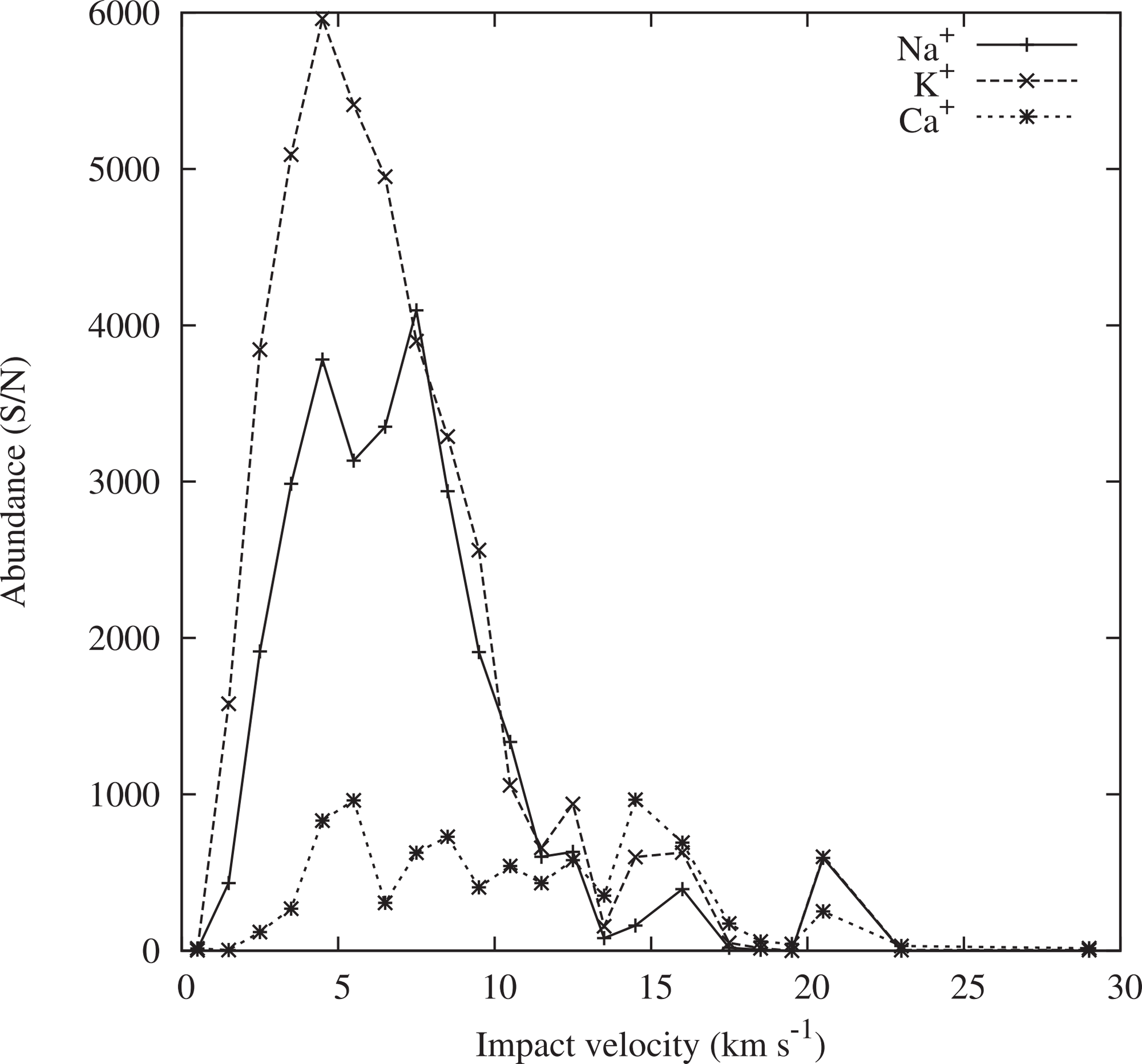
Na+
K+
Ca+
Abundance (S/N)
Impact velocity (km s-1)
0
1000
2000
3000
4000
5000
6000
0
5
10
15
20
25
30

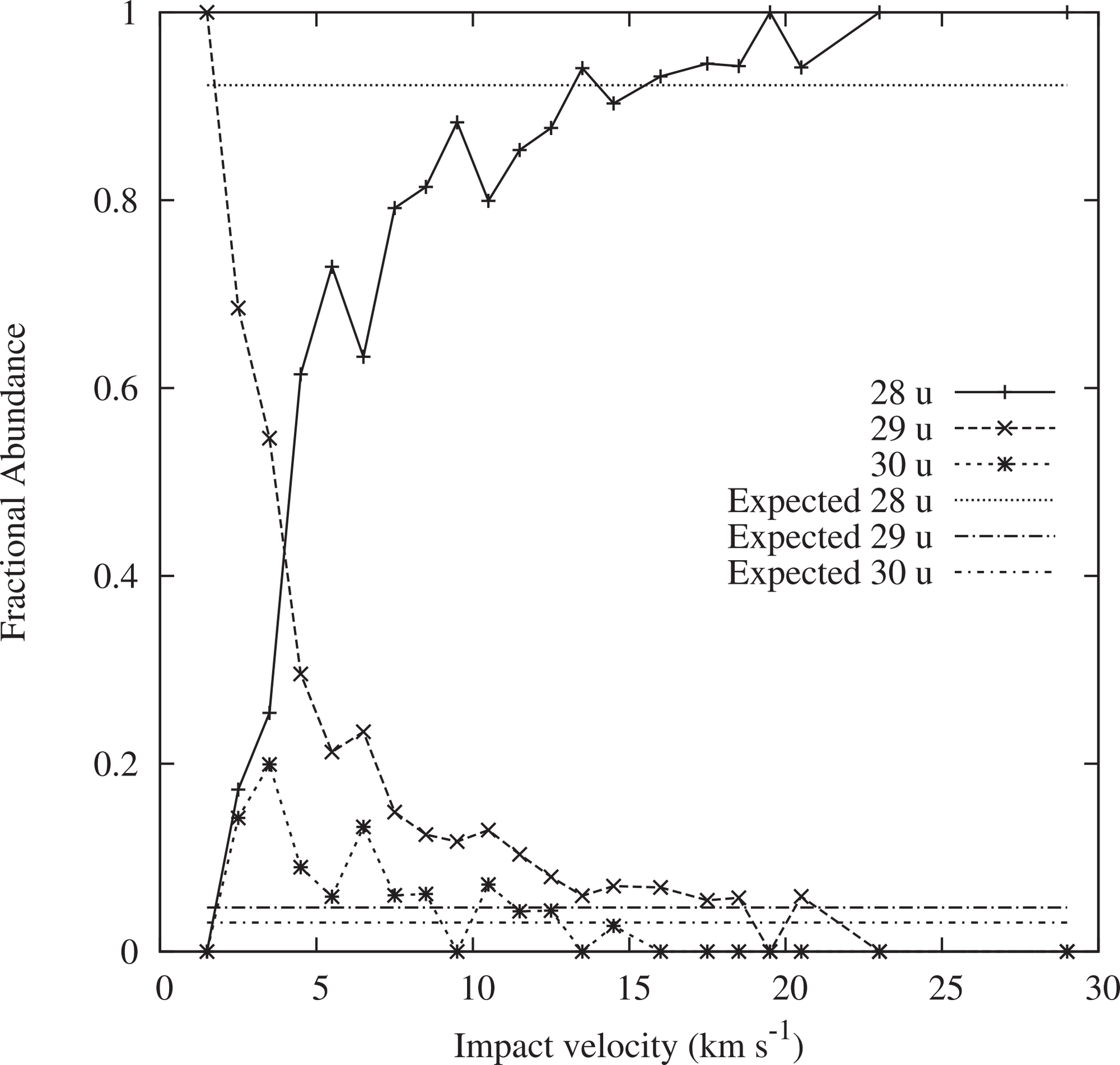
Fractional Abundance
Impact velocity (km s-1)
0
0.2
0.4
0.6
0.8
1
0
5
10
15
20
25
30
28 u
29 u
30 u
Expected 28 u
Expected 29 u
Expected 30 u

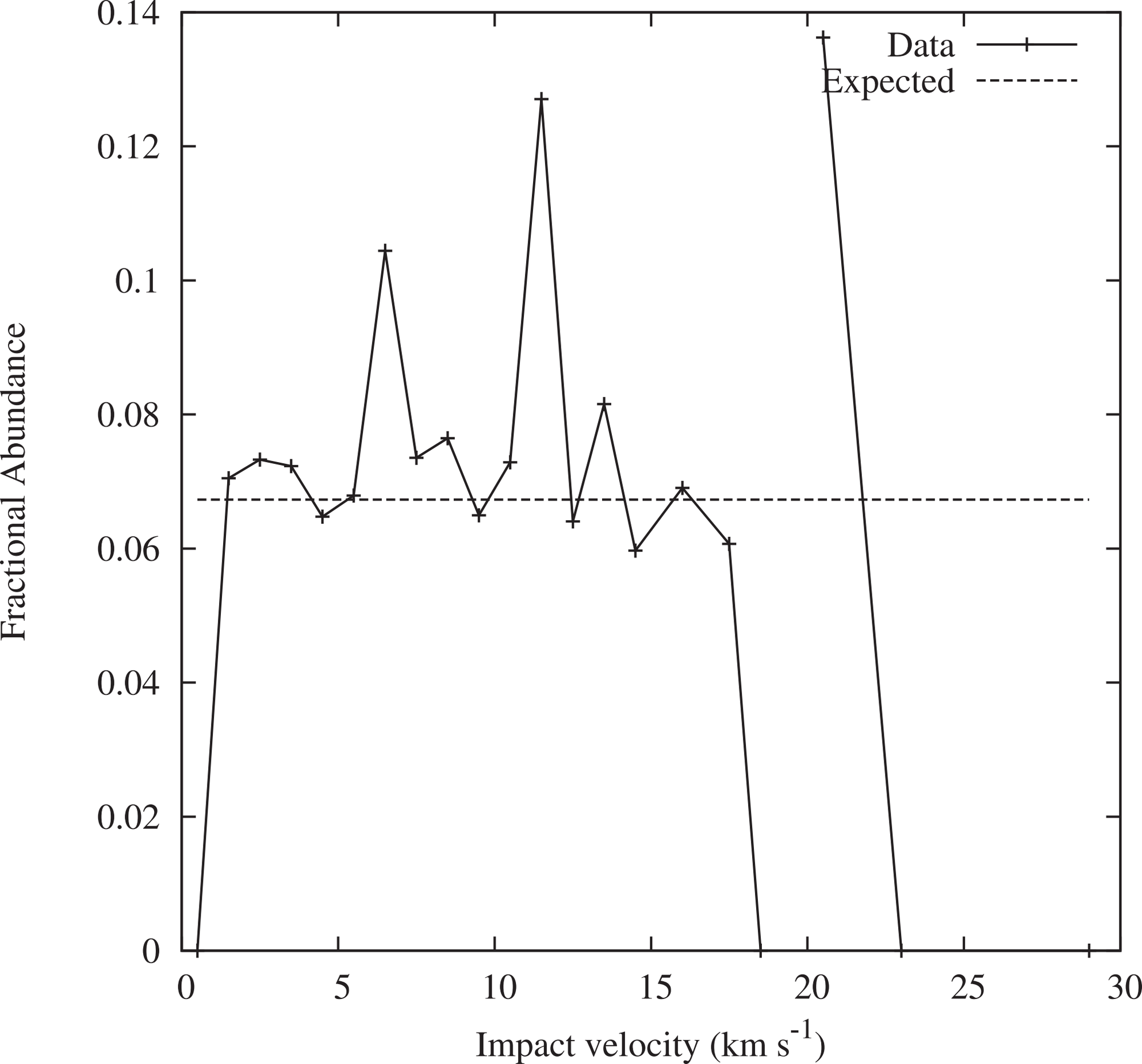
Data
Expected
Fractional Abundance
Impact velocity (km s-1)
0.14
0.12
0.1
0.08
0.06
0.04
0.02
0
0
5
10
15
20
25
30

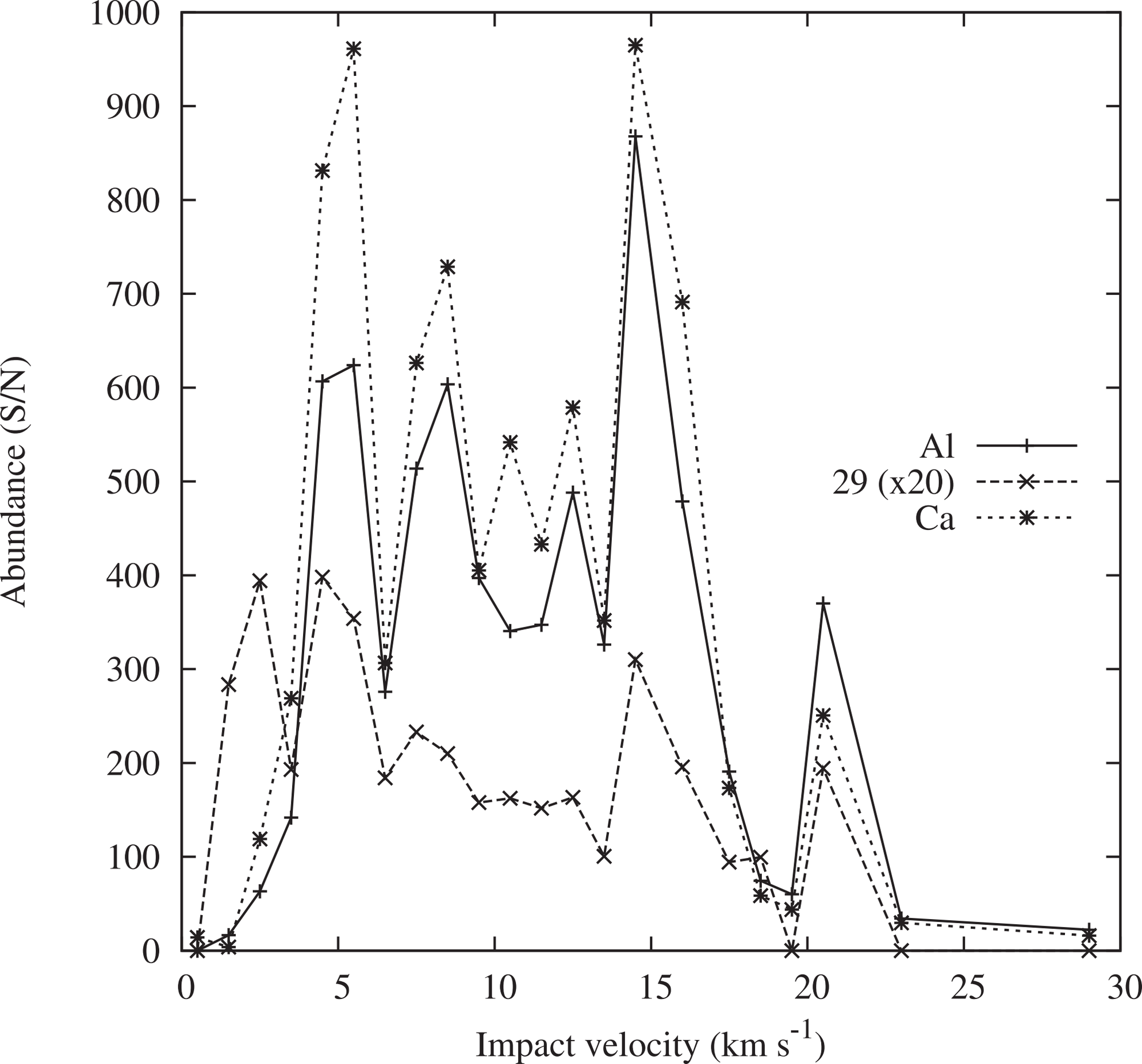
Abundance (S/N)
Impact velocity (km s-1)
Al
29 (x20)
Ca
0
100
200
300
400
500
600
700
800
900
1000
0
5
10
15
20
25
30

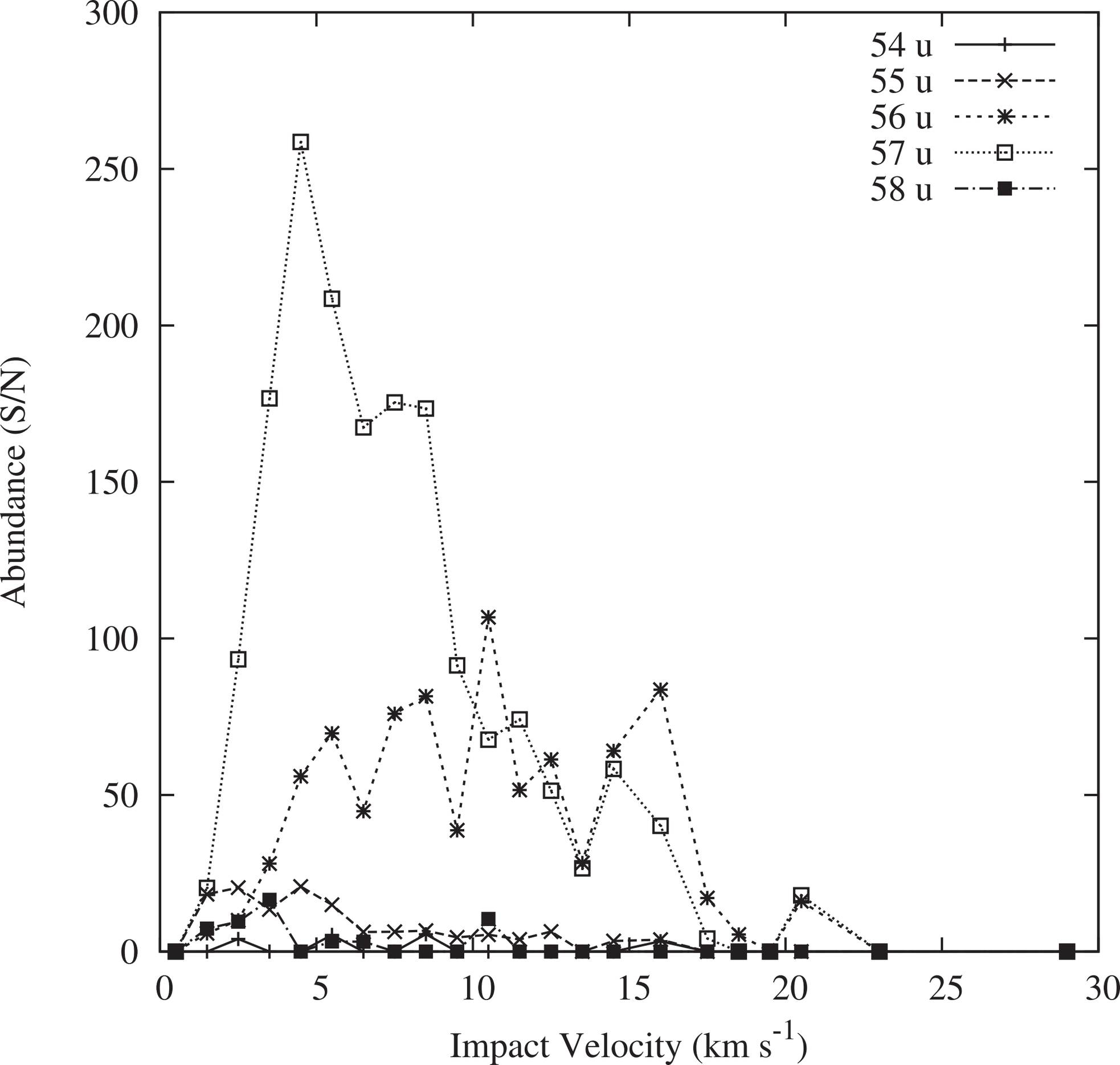
54 u
55 u
56 u
57 u
58 u
Abundance (S/N)
Impact Velocity (km s-1)
0
50
100
150
200
250
300
0
5
10
15
20
25
30

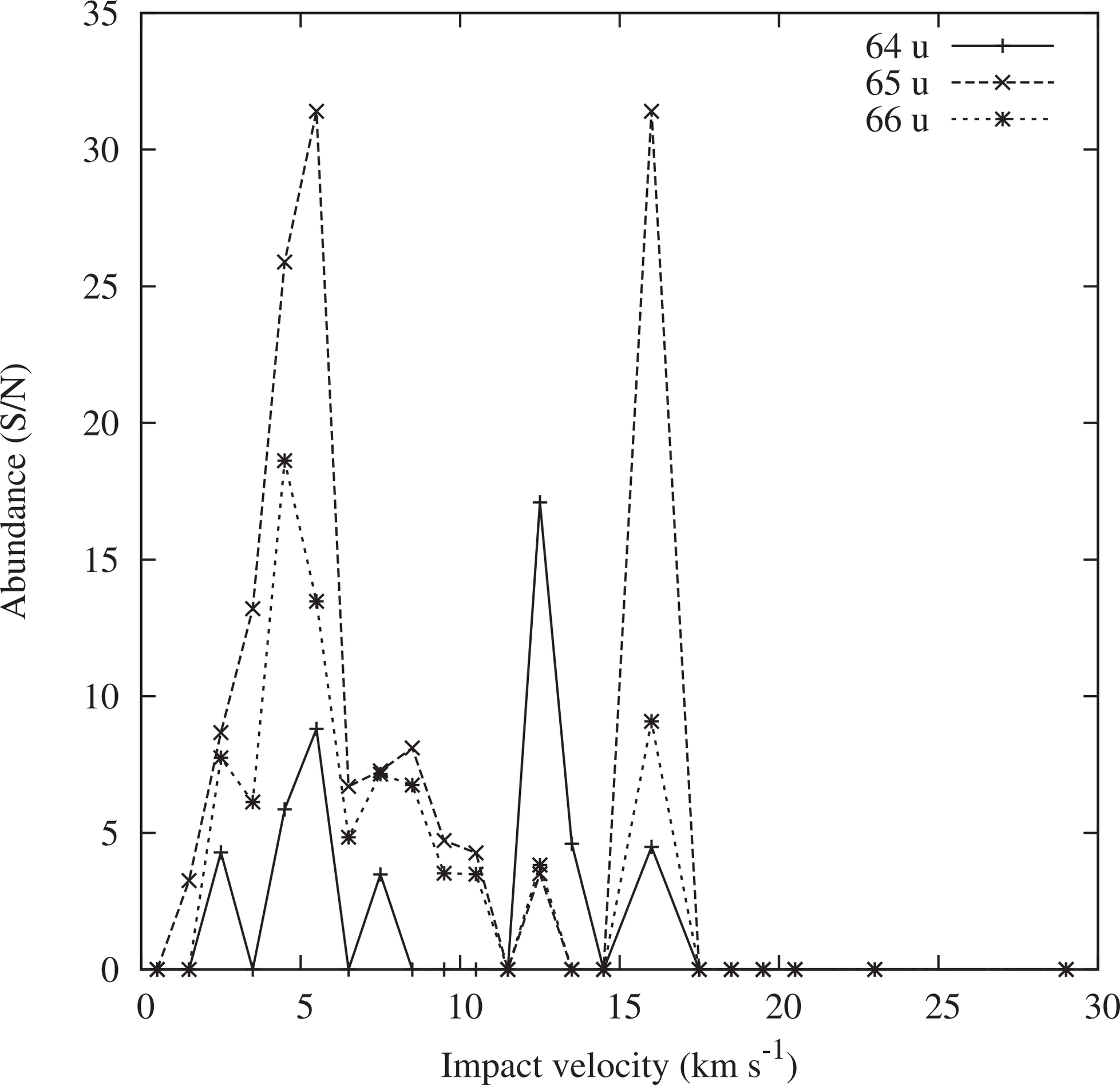
64 u
65 u
66 u
Abundance (S/N)
Impact velocity (km s-1)
0
5
10
15
20
25
30
35